

ALMA Lensing Cluster Survey: Dust mass measurements as a function of redshift, stellar-mass and star formation rate, from $z = 1$ to $z = 5$

Jean-Baptiste Jolly^{1,2}, Kirsten Knudsen², Nicolas Laporte³, Andrea Guerrero⁴, Seiji Fujimoto^{5,6}, Kotaro Kohno^{7,8}, Vasily Kokorev⁹, Claudia del P. Lagos¹⁰, Thiébaud-Antoine Schirmer², Franz Bauer^{11,12,13}, Miroslava Dessauge-Zavadsky¹⁴, Daniel Espada^{15,16}, Bunyo Hatsukade⁷, Anton M. Koekemoer¹⁷, Johan Richard¹⁸, Fengwu Sun¹⁹, and John F. Wu^{20,21}

¹ Max-Planck-Institut für extraterrestrische Physik, 85748 Garching, Germany

² Department of Space, Earth and Environment, Chalmers University of Technology, SE-412 96 Gothenburg, Sweden
e-mail: jbjolly@mpe.mpg.de

³ Aix Marseille Université, CNRS, CNES, LAM (Laboratoire d'Astrophysique de Marseille), UMR 7326, 13388 Marseille, France

⁴ Astronomy Department, Universidad de Concepción, Barrio Universitario S/N, Concepción, Chile

⁵ Cosmic Dawn Center (DAWN), Denmark

⁶ Niels Bohr Institute, University of Copenhagen, Jagtvej 128 DK-2200 Copenhagen N, Denmark

⁷ Institute of Astronomy, Graduate School of Science, The University of Tokyo, 2-21-1 Osawa, Mitaka, Tokyo 181-0015, Japan

⁸ Research Center for the Early Universe, Graduate School of Science, The University of Tokyo, 7-3-1 Hongo, Bunkyo-ku, Tokyo 113-0033, Japan

⁹ Kapteyn Astronomical Institute, University of Groningen, PO Box 800, 9700 AV Groningen, The Netherlands

¹⁰ International Centre for Radio Astronomy Research (ICRAR), M468, University of Western Australia, 35 Stirling Hwy, Crawley, WA 6009, Australia

¹¹ Instituto de Astrofísica, Facultad de Física, Pontificia Universidad Católica de Chile, Campus San Joaquín, Av. Vicuña Mackenna 4860, Macul Santiago, Chile, 7820436

¹² Centro de Astroingeniería, Facultad de Física, Pontificia Universidad Católica de Chile, Campus San Joaquín, Av. Vicuña Mackenna 4860, Macul Santiago, Chile, 7820436

¹³ Millennium Institute of Astrophysics, Nuncio Monseñor Sótero Sanz 100, Of 104, Providencia, Santiago, Chile

¹⁴ Observatoire de Genève, Université de Genève, 51 Ch. des Maillettes, 1290 Versoix, Switzerland

¹⁵ Departamento de Física Teórica y del Cosmos, Campus de Fuentenueva, Edificio Mecenas, Universidad de Granada, E-18071, Granada, Spain

¹⁶ Instituto Carlos I de Física Teórica y Computacional, Facultad de Ciencias, E-18071, Granada, Spain

¹⁷ Space Telescope Science Institute, 3700 San Martin Dr., Baltimore, MD 21218, USA

¹⁸ CRAL, Observatoire de Lyon, Université Lyon 1, 9 Avenue Ch. André, F-69561 Saint Genis Laval Cedex, France

¹⁹ Steward Observatory, University of Arizona, 933 N. Cherry Avenue, Tucson, 85721, USA

²⁰ Space Telescope Science Institute, 3700 San Martin Dr., Baltimore, MD 21218, USA

²¹ Department of Physics & Astronomy, Johns Hopkins University, 3400 N Charles St, Baltimore, MD 21218

Accepted November 15, 2024 (Submitted to A&A)

ABSTRACT

Context. Understanding the dust content of galaxies, its evolution with redshift and its relationship to stars and star formation is fundamental for our understanding of galaxy evolution. Dust acts as both a catalyst of star formation and as a shield for star light. State-of-the-art millimeter ground-based facilities like ALMA have made dust observation ever more accessible, even at high redshift. However dust emission is typically very faint, making the use of stacking techniques instrumental in the study of dust in statistically sound samples.

Aims. Using the ALMA Lensing Cluster Survey (ALCS) wide-area band-6 continuum dataset (~ 110 arcmin² across 33 lensing clusters), we aimed at constraining the dust mass evolution with redshift, stellar mass and star formation rate (SFR).

Methods. After binning sources according to redshift, SFR and stellar mass –extracted from an HST-IRAC catalog– we performed a set of continuum stacking analyses in the image domain using LINESTACKER on sources between $z = 1$ and $z = 5$, further improving the depth of our data. The large field of view provided by the ALCS allows us to reach a final sample of ~ 4000 galaxies with known coordinates and SED-derived physical parameters. We stack sources with SFR between 10^{-3} and $10^3 M_{\odot}$ per year, and stellar mass between 10^8 and $10^{12} M_{\odot}$, splitting them in different stellar mass and SFR bins. Through stacking we retrieve the continuum 1.2 mm flux, a known dust mass tracer, allowing us to derive the dust mass evolution with redshift and its relation with SFR and stellar mass.

Results. We observe clear continuum detections in the majority of the subsamples. From the non detections we derive $3\text{-}\sigma$ upper limits. We observe a steady decline in the average dust mass with redshift. Moreover, sources with higher stellar mass or SFR have higher dust mass on average, allowing us to derive scaling relations. Our results are mostly in good agreement with models at $z \sim 1 - 3$, but indicate typically lower dust-mass than predicted at higher redshift.

Key words. galaxies: evolution – galaxies: statistics – galaxies: ISM — ISM: dust

1. Introduction

Dust impacts both the direct evolution of galaxies as well as their observations in multiple ways. It is thought to be the main catalyst of H_2 formation (Wakelam et al. 2017), one of the main components of the molecular clouds in the interstellar medium (ISM) and hence one of the principal drivers of star formation (e.g. Scoville 2013). In addition to the direct effect on the physical properties of galaxies, dust also plays a critical role in astrophysical observations. The dust grains attenuating the starlight are consequently heated, and in turn re-radiate the energy at longer wavelengths, this is the so-called dust-obscured star formation (see for e.g. Casey et al. 2014; Hodge & da Cunha 2020; Zavala et al. 2021). As a consequence, the light coming from star-forming regions is typically dominated by dust continuum emission. The relationship between dust mass and other physical characteristics of galaxies have been intensely studied, for example, by studying dust-to-gas (atomic and molecular) or dust-to-metal ratios (e.g. Hunt et al. 2005; Draine et al. 2007; Engelbracht et al. 2008; Galametz et al. 2011; Magrini et al. 2011; Saintonge et al. 2013; Rémy-Ruyer et al. 2014; Combes 2018; Li et al. 2019; Shapley et al. 2020; Tacconi et al. 2020; Birkin et al. 2021; Popping & Péroux 2022; Popping et al. 2023), or dust mass versus star formation rate (SFR) (e.g. da Cunha et al. 2010; Casey 2012; Santini et al. 2014; Dudzevičiūtė et al. 2020, 2021).

Recent studies have shown that the proportion of dust-obscured star formation has evolved with redshift (Bouwens et al. 2020). It has been estimated to be a dominant fraction during the peak of the cosmic star formation history. However, it appears to have accounted for only $\sim 20\% - 25\%$ of the total star formation at redshift $z = 6 - 7$ (see Zavala et al. 2021). Similarly, the overall cosmic dust density has been evidenced to peak around $z \sim 1 - 2$ with a rapid decline at higher redshift (see for example Driver et al. 2018; Magnelli et al. 2020; Pozzi et al. 2020; Dudzevičiūtė et al. 2021). Furthermore, massive dust reservoirs have been detected in massive high-redshift galaxies (e.g. Bertoldi et al. 2003; Valiante et al. 2009; Venemans et al. 2012; Watson et al. 2015; Laporte et al. 2017; Tamura et al. 2019, 2023). While this is probably not the case for more typical, less massive high-redshift galaxies, it highlights the importance of studying the evolution of dust mass with redshift.

Millimeter or sub-millimeter emission has been proposed to be a tracer of dust mass (Scoville et al. 2014, 2016, 2017), with the assumption that the emission is optically thin and measured far from the peak of the dust spectral energy distribution. The Atacama Large Millimeter/Submillimeter Array (ALMA) has become instrumental in the quest to study dust mass in lower-mass galaxies and its evolution in the mm and sub-mm bands. With large surveys and high-redshift single target observations becoming progressively more accessible (e.g. Knudsen et al. 2016; Walter et al. 2016; González-López et al. 2017, 2020; Laporte et al. 2017; Béthermin et al. 2020; Aravena et al. 2020) the evolution of dust is studied in increasingly statistically sound samples.

However, observations of high-redshift galaxies are typically biased by construction towards the observation of the brightest sources (Malmquist bias). To draw a complete picture of dust evolution with redshift it is necessary to also study galaxies with lower intrinsic luminosities. Gravitational lensing can be used as a tool to enhance the signal from faint galaxies without the need for excessive integration time. Similarly, tools like stacking can statistically improve the signal-to-noise ratio (S/N) drastically when studying large samples. With the help of both gravitational

lensing and stacking, it is hence possible to push the limit of observations toward sources with lower intrinsic dust luminosity.

In this paper we present the stacking analysis of 10386 gravitationally lensed galaxies from the ALMA Lensing Cluster Survey (ALCS) at $z > 1$ (cluster and field sources at $z \lesssim 1$ are studied in a separate paper: Guerrero et al. (2023)). By binning galaxies by redshift, and further splitting them according to their stellar mass or SFR, we study the evolution of the dust mass with redshift, and its scaling relation with stellar mass and SFR. Besides, we also integrate the contribution from all galaxies – in each redshift bin – to assess the evolution of the cosmic dust density.

In Section 2 we describe the overall data set, the catalog and the different subsamples. In Section 3 we describe both the stacking method, performed using LINESTACKER (Jolly et al. 2020), as well as the processes involved in the dust mass calculation. In Section 4 we present our results and discuss them in Section 5. Finally in Section 6 we present a summary of this paper. In the appendix we show alternative stacking procedures as well as some extra details on the main analysis.

Throughout the paper, we assume a Λ CDM cosmology with $\Omega_m = 0.3$, $\Omega_\lambda = 0.7$ and $H_0 = 70 \text{ km s}^{-1} \text{ Mpc}^{-3}$. All magnitudes are quoted in the AB system, such that $M_{AB} = 23.9 - 2.5 \log_{10}(S_\nu [\mu\text{Jy}])$.

2. Data and sample

2.1. ALCS

The ALMA Lensing Cluster Survey (ALCS) is a large ALMA program accepted in cycle 6 (Project ID: 2018.1.00035.L; PI: K. Kohno). It observed 33 lensing clusters in band 6 ($\lambda \sim 1.2 \text{ mm}$), spanning $\sim 110 \text{ arcmin}^2$ (primary beam (PB) > 0.5). The clusters are distributed as follow: 16 from RELICS (the Reionization Lensing Cluster Survey Coe et al. 2019), 12 from CLASH (the Cluster Lensing And Supernova survey with Hubble Postman et al. 2012), and 5 from the Frontier Fields survey (Lotz et al. 2017). Observations were carried out between December 2018 and December 2019 (cycles 6 and 7) in compact array configurations C43-1 and C43-2, in a double frequency window setup, observing both from 250.0 to 257.5 GHz and from 265.0 to 272.5 GHz, for a total bandwidth of 15 GHz. When available, the ALCS data were concatenated with existing ALMA data, notably the ALMA Frontier Fields Survey (Project ID: 2013.1.00999.S, PI: Bauer and Project ID: 2015.1.01425.S: PI: Bauer). The data were reduced and calibrated using the Common Astronomy Software Applications (CASA, McMullin et al. 2007) package version 5.4.0 for the 26 clusters observed in cycle 6 and v5.6.1 for the remaining clusters observed in cycle 7. Throughout this paper, we use natural-weighted, primary-beam-corrected, and uv -tapered continuum maps, with a tapering parameter of 2 arcsec (the full width at half maximum of the synthesized beam is 2 arcsec; with a corresponding pixel size of 0.16 arcsec). uv -tapered maps have been chosen over natural resolution maps to ensure beam-size homogeneity of the different images when stacking. The average RMS of the maps is $\sim 63 \mu\text{Jy}/\text{beam}$, see Table 1 for the detailed RMS of each map. Full description of the survey can be found in Kohno et al. (2023).

2.2. Source catalogue

We extracted the positions, redshifts, physical characteristics (SFRs and stellar masses) as well as lensing magnifications of

galaxies at $1 \leq z \leq 5$ from the HST-IRAC catalog presented in [Kokorev et al. \(2022\)](#). When available, spectroscopic redshifts are used in place of photometric redshifts. While the SFRs and stellar masses extracted from the [Kokorev et al. \(2022\)](#) catalog are not corrected for magnification, the SFRs and stellar masses presented in this paper are always the intrinsic ones, i.e. corrected for magnification.

From the full catalog we select only the sources that (the number of remaining sources is indicated in *italic* after each step): (i) have defined redshifts and magnifications, and are not tagged with bad photometry (*bad_phot* \neq 1) – 1888977 (ii) have redshift uncertainties ($|z_{160} - z_{840}|$) below 0.4 – 76728 (iii) have $10^8 \leq M_*/M_\odot \leq 10^{12}$ and $0.001 \leq \text{SFR}/(M_\odot/\text{year}) \leq 10^3$ – 51355 (iv) have H-band magnitudes above 24, to avoid contamination from blue faint galaxies – 50983 (v) have associated PB values higher than 0.5 – 13403 (vi) have a $z < 5$ – 12980 (vii) have a magnification factor below 100 – 12967 (viii) have a $z \geq 1$ – 4103, as lower redshift sources as well as cluster sources were presented in a separate paper, [Guerrero et al. \(2023\)](#). In total, our full sample finally adds up to a total of 4103 sources. [Table 1](#) presents the distribution of sources in the 33 clusters observed in the ALCS as well as the RMS of each map.

[Figure 1](#) shows the distributions of stellar mass, SFR, magnification and redshift in the final sample. [Figure 2](#) shows the distance of each galaxy from the galaxy main sequence (MS) as a function of redshift – $\Delta(\text{MS}) = \log(\text{SFR}_{\text{MS}}) - \log(\text{SFR})$ with SFR_{MS} the expected SFR for a galaxy with the same stellar mass and on the MS (according to [Speagle et al. 2014](#)), and SFR the actual SFR of the galaxy. The sample shows an over-density of quiescent galaxies (as also shown in [Guerrero et al. 2023](#)). To assess the impact of quiescent galaxies on the stack we also stacked every sample after first excluding galaxies with $\Delta\text{MS} < -0.5$, see Appendix.

To further evaluate the completeness and reliability of the sample we compare its stellar mass function (SMF) to the one derived in the COSMOS2020 sample ([Weaver et al. 2022a,b](#)). To derive the SMF of our sample we count –for each cluster separately– the number of galaxies in a given redshift bin and divide by the corresponding volume, corrected for the mean magnification of the sources in the studied bin. The comparison is shown on [Figure 3](#). The studied sample seems to present an over-density of sources at $z > 4$, and an under-estimation of sources in the $2 < z \leq 3$ bin, especially at high-masses. This might be due to the miss-identification of low redshift sources as high-redshift ones, as also discussed in [Guerrero et al. \(2023\)](#). [Kokorev et al. \(2022\)](#) compared the spectroscopic redshifts, known for ~ 7000 galaxies, to the photometric redshifts they derived: while $\sim 80\%$ of the redshifts agree reasonably well, the remaining $\sim 20\%$ present large to sometimes catastrophic ($\Delta z > 3$) errors, mainly due to the confusion of the Lyman, Balmer, and 4000 Å breaks. In addition, an under-evaluation of the survey volume (coming from an over-evaluation of the corresponding magnification) might also artificially boost the source density. The potential impact of the derived SMF are further discussed in [Section 5](#).

2.3. Subsamples

To study the evolution of dust mass across redshift we separated the sources in four redshift bins: $1 \leq z < 2$, $2 \leq z < 3$, $3 \leq z < 4$ and $4 \leq z < 5$. We additionally split sources according to either their SFRs or stellar masses in the following bins: (i) SFR, (upper and lower limits in $M_\odot \text{yr}^{-1}$): $0.001 \leq \text{SFR} \leq 1$, $1 <$

Table 1. Number of stacked sources in each cluster, and maps RMS.

Cluster name	Number of stacked sources	Maps RMS ($\mu\text{Jy}/\text{beam}$)
HFF clusters:		
Abell2744	418	51
Abell370	346	47
AbellS1063	369	53
MACSJ0416.1-2403	473	55
MACSJ1149.5+2223	325	64
CLASH clusters:		
Abell209	74	63
Abell383	63	61
MACS0329.7-0211	62	71
MACS0429.6-0253	37	92
MACS1115.9+0129	51	63
MACS1206.2-0847	127	53
MACS1311.0-0310	38	62
MACS1423.8+2404	101	65
MACS1931.8-2635	80	56
MACS2129.4-0741	116	47
RXJ1347-1145	95	53
RXJ2129.7+0005	31	40
RELICS clusters:		
Abell2163	11	50
Abell2537	52	69
Abell3192	91	73
AbellS295	39	74
ACTCLJ0102-49151	253	72
MACSJ0035.4-2015	72	52
MACSJ0159.8-0849	69	63
MACSJ0257.1-2325	67	83
MACSJ0417.5-1154	135	84
MACSJ0553.4-3342	157	65
PLCKG171.9-40.7	28	73
RXCJ0032.1+1808	81	71
RXCJ0600.1-2007	66	57
RXCJ0949.8+1707	38	62
RXCJ2211.7-0350	52	78
SMACSJ0723.3-7327	86	66
Total: 4103		Average: 63

$\text{SFR} \leq 10$, $10 < \text{SFR} \leq 50$, $50 < \text{SFR} \leq 100$ and $100 < \text{SFR} \leq 1000$; (ii) stellar mass, (M_* , upper and lower limits in M_\odot): $10^8 \leq M_* \leq 10^9$, $10^9 < M_* \leq 10^{10}$, $10^{10} < M_* \leq 10^{11}$ and $10^{11} < M_* \leq 10^{12}$. The total number of sources in each subsample can be found on [Table 2](#). Further, the distribution of SFR and stellar mass in each subsample can be found in the appendix, on [Figures C.1](#) and [C.2](#).

One should note that sources individually detected in the ALCS data are not excluded from the samples. We decided to discriminate solely on the properties mentioned above to derive average properties of the population, and, in that regard, the 1.2 mm continuum flux density of individual sources should not be a criterion of exclusion from our samples. To assess the impact of the 1.2 mm flux distribution in our samples, we perform median stacking as well as bootstrapping analyses, alongside the main mean-stacking analyses, see [Sections 3.4](#) and [4.2](#).

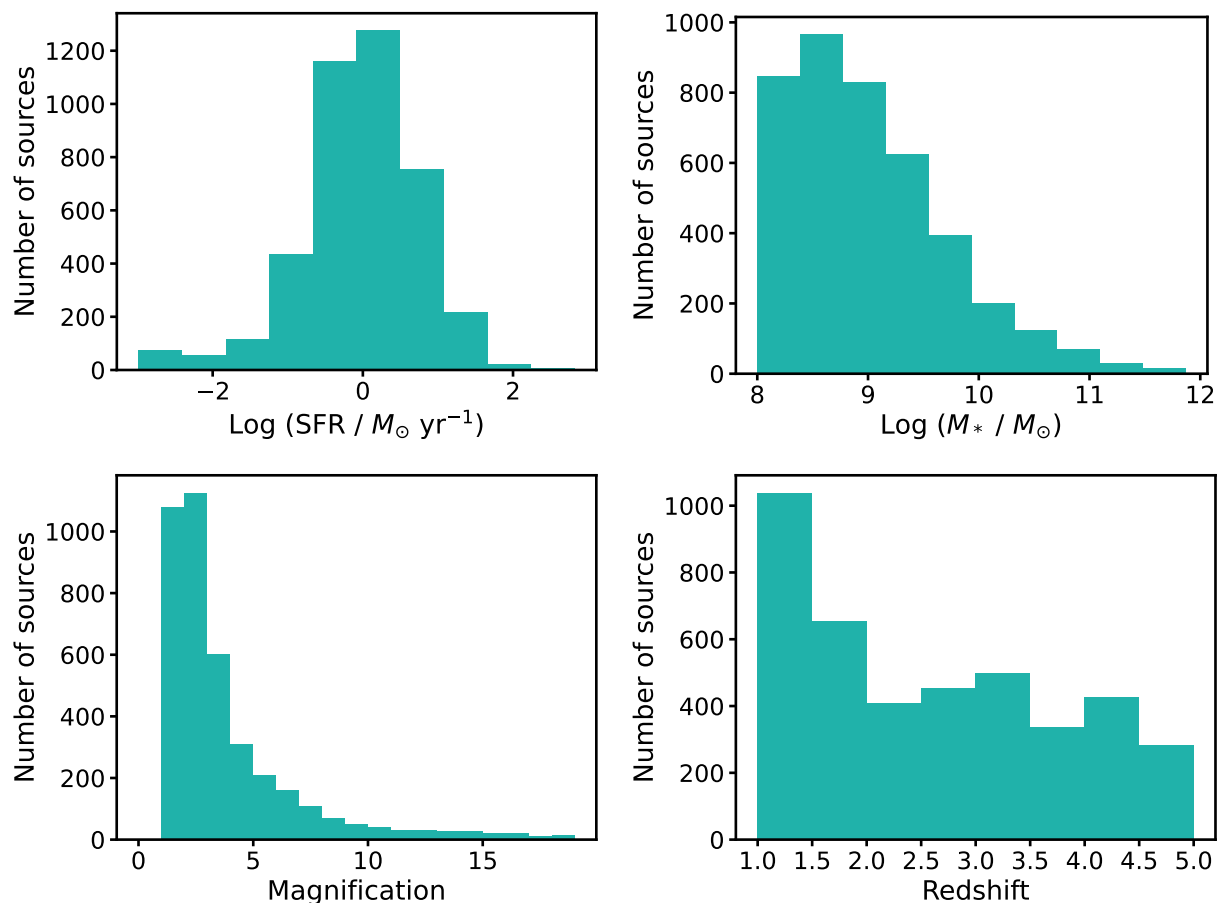


Fig. 1. Distribution of the main physical properties of interest in the whole sample. SFRs and stellar masses are corrected for magnification.

Table 2. Number of stacked sources in each subsample.

	$1 \leq z < 2$	$2 \leq z < 3$	$3 \leq z < 4$	$4 \leq z < 5$	Total
$8 \leq \log(M_*) \leq 9$	1004	521	432	375	2332
$9 < \log(M_*) \leq 10$	508	295	309	256	1368
$10 < \log(M_*) \leq 11$	154	43	84	60	341
$11 < \log(M_*) \leq 12$	27	4	11	20	62
$0.001 \leq \text{SFR} \leq 1$	1046	441	306	250	2043
$1 < \text{SFR} \leq 10$	529	377	455	394	1755
$10 < \text{SFR} \leq 50$	113	43	67	58	281
$50 < \text{SFR} \leq 100$	5	1	1	5	12
$100 < \text{SFR} \leq 1000$	-	1	7	4	12

3. Methods

3.1. Stacking

Stacking was done using LINESTACKER (Jolly et al. 2020), in single channel mode (to perform continuum stacking), on uv -tapered images (see Section 2.1). Sources were stacked pixel to pixel using mean stacks without weights (median stacks are also performed, see Section 4.2). Stacking was operated with stamp sizes of 9.76×9.76 arcsec² (61×61 pixels). Sources were spatially aligned using the position extracted from the Kokorev et al. (2022) catalog. Stacked flux in Jy was retrieved by integrating the continuum flux in a central circular region of the stack stamp, with a radius $R_{\text{integ}} = 2''$ (12.5 pixels), corresponding to the synthesized beam size, and dividing it by the beam size in pixel units.

To compute the RMS associated to each stacked cube a random set of source-free coordinates are drawn for each stacking position. An empty stack is then generated from the set of random coordinates (see Jolly et al. 2020) with the same characteristics as the normal stacks (i.e. stamp size and number of targets). This process is performed 1000 times for each subsample. The standard deviation across all stack stamps is then computed and used to derive the RMS associated to each stack cube.

When the flux in the central region of the stack stamp is lower than 3 times its associated RMS, a 3σ upper limit is used in place of the integrated flux to compute M_{dust} .

3.2. Magnification corrections

The averaged 1.2 mm fluxes extracted from each stack maps are corrected for the mean magnification of sources in the stack sub-

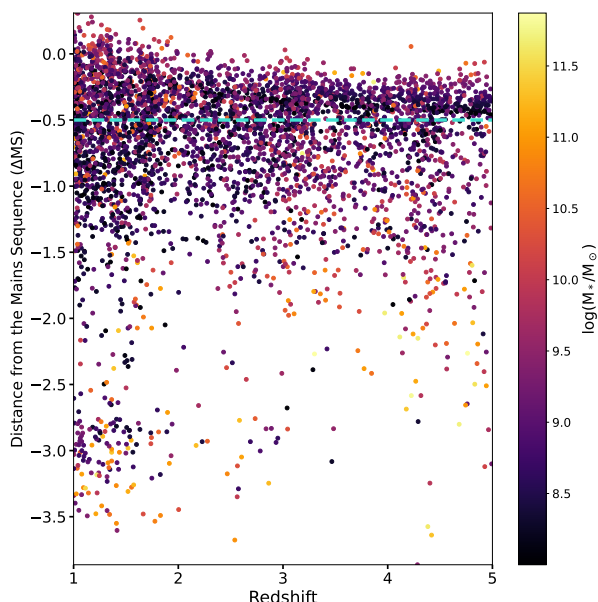


Fig. 2. Distance from the main sequence $\Delta(\text{MS}) = \log(\text{SFR}_{\text{MS}}) - \log(\text{SFR})$ (from Speagle et al. 2014) as a function of redshift, for the galaxies in the full sample. Points are color coded for their stellar mass. A dashed line at $\Delta(\text{MS}) = -0.5$ highlights the region of exclusion of quiescent galaxies (see Appendix).

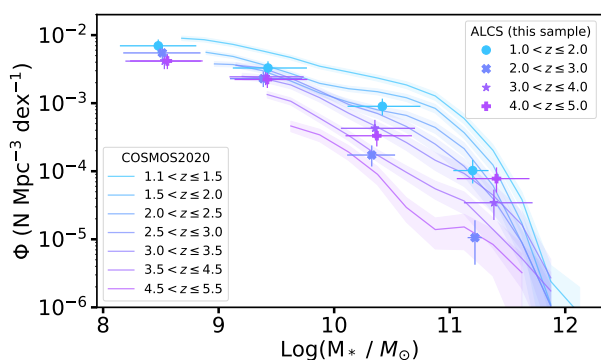


Fig. 3. Comparison between the SMF of the COSMOS2020 sample (Weaver et al. 2022a,b) and the SMF of the sources studied in this paper. The SMF is obtained by counting the galaxies in each redshift bin and dividing by the corresponding volume, corrected for the mean magnification of the sources in each bin, for each cluster separately. The error bars correspond to the 16th to 84th percentile of the stellar mass of the sources in the sample, and the impact of the 20% error on the magnification on the total volume.

sample, the final flux is hence computed as: $F_{\text{final}} = \frac{F_{\text{stack}}}{\bar{\mu}}$, where F_{final} is the final flux used to compute the dust mass (see Section 3.3), F_{stack} is the flux obtained from the stacked map, and $\bar{\mu}$ is the average magnification of each source in the subsample. Alternatively, each source could be corrected for its magnification before stacking: $F_{\text{final}} = F_{\text{corrected stack}}$, where $F_{\text{corrected stack}}$ is the flux obtained from the stack of the individually magnification-corrected maps: $\text{Map}_{\text{stack}} = \sum_{i=1}^n \frac{\text{Stamp}_i}{\mu_i}$, where $\text{Map}_{\text{stack}}$ is the stacked map obtained from individually magnification-corrected stamps (from which $F_{\text{corrected stack}}$ is obtained), n is the number of sources in the subsample, Stamp_i is the map-stamp associated to source i and μ_i is the magnification associated to source i . The reason why we decided to correct for the average magnification of the sample after stacking is the following: the signal

in each stack stamp consists of both the flux from the source, which is gravitationally magnified, and some noise, which is independent of the magnification. By correcting each stack stamp for its associated magnification, one corrects both the flux from the source and the foreground noise. The efficiency of stacking is based on the fact that the noise is random and approximately similar in every stack stamp. By down-scaling the noise in each stamp by a different number (unrelated to the noise properties), one might effectively reduce the efficiency and reliability of the stacking analysis. However, by correcting the final stack with the average magnification, the analysis would be biased toward high-magnification sources. Correcting each stamp individually pre-stacking should avoid this bias, we hence repeated our analysis with this correction method. The 1.2 mm fluxes derived in both cases are very consistent, with values overlapping within the error margins.

3.3. Measuring M_{dust}

To derive dust masses using the 1.2 mm continuum flux extracted from each stacking stamp, we use a single modified blackbody curve, under the approximation of an optically thin regime, following Kovács et al. (2010) and Magnelli et al. (2020) we define M_{dust} as:

$$M_{\text{dust}} = \frac{5.03 \times 10^{-31} (S_{\nu_{\text{obs}}}/f_{\text{CMB}}) D_{\text{L}}^2 \left(\frac{\nu_0}{\nu_{\text{rest}}} \right)^{\beta}}{(1+z)^4 B_{\nu_{\text{obs}}}(T_{\text{obs}}) \kappa_{\nu_0}}, \quad (1)$$

where M_{dust} is the dust mass in M_{\odot} , $S_{\nu_{\text{obs}}}$ is the flux at the observed frequency in Jy (and corrected for the average magnification, as explained in Section 3.2), $\nu_{\text{obs}} = \nu_{\text{rest}}/(1+z)$ is the observed frequency, f_{CMB} is the correction factor to account for the cosmic microwave background (CMB, see details further in the text), D_{L} is the luminosity distance in meter at redshift z , $B_{\nu_{\text{obs}}}(T_{\text{obs}})$ is Planck's blackbody function in Jy sr^{-1} at the observed temperature T_{obs} ($T_{\text{obs}} = T_{\text{rest}}/(1+z)$), κ_{ν_0} is the photon cross section to mass ratio of dust in $\text{m}^2 \text{kg}^{-1}$ and β is the dust emissivity index. $S_{\nu_{\text{obs}}}$ is obtained by integrating over a fixed circular region in the center of the stack stamp (see Section 3.1).

Following Magnelli et al. (2020) and Pozzi et al. (2021) we decided to use a single cold component to account for the dust temperature, and used a mass weighted dust temperature of $T_{\text{rest}} = 25$ K. While the total dust in galaxies is thought to consist of a warmer ($20 < T < 60$ K) and a colder ($T < 30$ K) component, studies of local galaxies have shown that the cold component is responsible for most of the dust budget (from 96% to 99%, see Orellana et al. 2017) and for the majority of the Rayleigh-Jeans emission (see also Shivaei et al. 2022, for a study of the contribution of the cold and warm dust components to the dust continuum emission at $z \sim 2$). Scoville et al. (2014, 2016, 2017) argue that this approximation should still be valid in higher redshift galaxies. We decided to adopt $T_{\text{rest}} = 25$ K at all redshifts probed by our analyses, but one should note that dust masses go as T^{-1} , meaning that our dust mass results are effectively highly dependent on the estimated dust temperature, and that the masses derived in our analyses could be off by factors of a few if the assumed dust temperature is not correct (see Section 5).

While choosing an evolving dust temperature with redshift could seem more appropriate, we decided to stick to a fixed value to allow easier comparison with similar previous studies. We used $\beta = 1.8$, the Galactic dust emissivity index measurement from the Planck data (Planck Collaboration et al. 2011) which

also correlates well with values observed in high-redshift galaxies (e.g. Chapin et al. 2009; Magnelli et al. 2012; Faisst et al. 2020). Theoretical studies predict values for β ranging from 1.5 to 2.0 (e.g. Draine 2011), similarly observational studies such as Faisst et al. (2020) find β values between 1.6 and 2.4 (with a median value of 2.0). The effect of β is however less impactful than the choice of dust temperature and we find that choosing $\beta = 1.5$ (or 2.0) would only modify our results by $\sim 9\%$ at $z = 1.5$ and $\sim 15\%$ at $z = 5.5$. We used $\kappa_{\nu_0} = 0.0431 \text{ m}^2 \text{ kg}^{-1}$ with $\nu_0 = 352.6 \text{ GHz}$ (Li & Draine 2001; Magnelli et al. 2020). See Section 5 for a more complete discussion of the choice of parameters for the dust mass computation.

Following da Cunha et al. (2013) we corrected our flux measurements for the effect of CMB. First, we correct our dust temperature for the extra heating due to the CMB (following Equation 12 of da Cunha et al. 2013). This effect is minor, as the dust temperature is only increased by $\sim 3\%$ at $z = 6$ (the effect being even less important at lower redshift). Second, and most importantly, the CMB acts as a bright observing background, leading to an underestimation of the total flux. This is corrected by following Equation 18 of da Cunha et al. (2013). This effect is much more important, as it yields an upward measurement to our results ranging from ~ 1.03 at $z \sim 1$ to ~ 1.31 at $z \sim 6$.

3.4. Uncertainty computation

To compute the overall uncertainties associated to our measurements, we combined different sources of uncertainties. The first is the direct RMS from each stack analysis (computed from source-free stacks of each subsample, see Section 3.1). In addition, in stacking analyses one should account for the intrinsic flux distribution of the sources in the sample. To do so, we perform a bootstrapping analysis for each subsample. In each subsample, the dust mass is re-computed 1000 times, each time with a different sample, randomized from the original subsample without replacement (see Jolly et al. (2020) for a detailed description of the bootstrapping routine included in LINESTACKER). The distribution of the dust masses computed in this manner are shown on Figures D.1 and D.2, where we also show the dust mass obtained from the original subsample (black vertical line). The peaks and shapes of the distributions are overall consistent with the values derived from the original samples. However, one can note that the peak of the distributions are, in most of the subsamples, slightly lower than the original stacks. Similarly, some distributions present a faint tail toward higher dust masses. These 2 informations combined hint for a skewed distribution, which can be easily explained from the presence of individual detections in the samples. These effects are small however, and should be well represented by the associated uncertainties on dust mass measurements.

From the distributions derived from of each bootstrapping analyses we extract the 16th to 84th percentile (see Figures D.1 and D.2) that we sum quadratically with the stack RMS¹. In addition, given that the redshift is used multiple times in equation 1, its 16th to 84th percentile in each subsample is used to propagate the associated uncertainty on the dust mass computation. Finally, following Sun et al. (2022) and Fujimoto et al. (2023) we use a magnification uncertainty of 20% of the magnification

associated to each subsample, and propagate it to the aforementioned errors.

The 16th and 84th percentile of the (magnification corrected) SFRs and stellar masses in each subsample are used to compute the error associated to the SFRs and stellar masses.

The combination of these measurements uncertainties are used to plot the error bars on the different figures shown in this work. However, only the RMS associated to each cube is used to qualify a detection or an upper limit (as stated in section 3.1).

4. Results

4.1. Mean stacking results, dust continuum detection

The standard deviation in stack stamps reaches levels as low as $\sim 4.3 \times 10^{-3} \text{ mJy}$ per beam, in the $z = 1 - 2$ bin, of the lowest stellar mass and SFR subsamples (both containing ~ 1000 sources). The total flux in the central circular aperture of 2 arcsec radius varies between $\sim 1.78 \times 10^{-2} \text{ mJy}$ and $\sim 1.04 \text{ mJy}$ for stack detections (flux above 3σ , not corrected for magnification). Securely extracted dust masses (with S/N above 3σ) range from $\sim 2.8 \times 10^6 M_\odot$ to $\sim 2.56 \times 10^8 M_\odot$ (after magnification correction). Figures 7 and 8 show the stacked maps obtained for each of the subsamples, from which the results presented below are extracted.

The evolution of dust mass with stellar mass and redshift is shown on Figure 4, and tabulated on Table 3. While detections in the lowest redshift bin ($1 < z < 2$) indicate a clear linear relationship between $\log(M_{\text{dust}})$ and $\log(M_*)$, the other redshift bins are less regular (see left panel of Figure 4). When comparing to other works (Santini et al. 2014; da Cunha et al. 2015; Kirkpatrick et al. 2017; Shivaei et al. 2022, also plotted on the figures), our data points are typically below other measurements (individual detections and stacks). This behavior is however strongly reduced when excluding quiescent galaxies from the stacks (see Appendix), highlighting that quiescent galaxies might have lower dust masses at the same stellar mass.

The $\log(M_{\text{dust}}) - \log(\text{SFR})$ relation seems to follow a similar trend of increasing dust mass with increasing SFR, but with a clearer linear relation across redshift (though there is a higher number of non-detection, see left panel of Figure 6 and stacking results tabulated in Table 4). Hinting that SFR might be a better suited than stellar mass to trace the dust mass. When comparing to previous works (Santini et al. 2014; da Cunha et al. 2015; Kirkpatrick et al. 2017; Shivaei et al. 2022) one can see that our measurements follow a similar trend as the one already observed, reaching however so far mostly unexplored regimes.

When looking at the evolution of dust mass with redshift (see the right panels of Figures 4 and 6 and Figure 5), one can see a relatively clear linear trend, indicating a decrease in dust mass with increasing redshift.

By fitting quadratic functions to the data shown on Figures 4 and 6, we derive scaling relations between: M_{dust} and M_* at fixed z ; M_{dust} and z at fixed M_* ; M_{dust} and SFR at fixed z ; and M_{dust} and z at fixed SFR. Fits are performed using detections only (ignoring upper limits), and only when the number of data points is ≥ 3 . The results from the fits are summarized in Table 5, and plotted on Figures B.1 and B.2

4.2. Median stacking analysis

To better assess the effect of the population distribution on the derived dust mass we also performed median-stacks, in the same way as the average stacks presented in Section 3.1. The overall

¹ One should note that the bootstrap analysis is also affected by the RMS of the stacked images. The two errors being hence correlated, one should in principle not add them quadratically. This is an approximation that should slightly over-estimate the error computation.

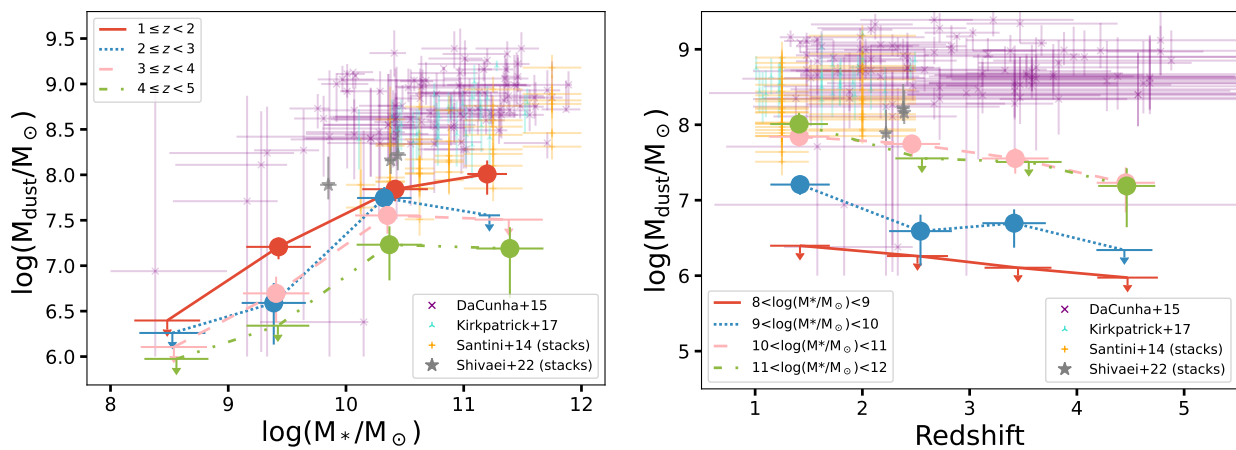


Fig. 4. (left) Average dust mass as a function of the stellar mass in each redshift bin. Circles represent detections (above 3σ) while down pointing arrows represent 3σ upper limits. Error bars on the dust mass detections are computed using a combination of different errors, see Section 3.4. Error bar along the x-axis represent the 16th to 84th percentile of parameter’s distribution in the stacked sample. (right) Similar to the left panel but plotting as a function of redshift in each stellar mass bin. Also shown for comparison: individual dust mass measurements detections da Cunha et al. (2015); Kirkpatrick et al. (2017) and stacking measurements from Santini et al. (2014); Shivaiei et al. (2022).

Table 3. Stacking results in stellar mass subsamples. When the central flux is lower than 3 times the rms of the corresponding stack map: the 3σ upper limit is shown in place of the dust mass. Errors on the computed dust mass correspond to the quadratic sum of the standard deviation computed from empty stacks with the uncertainties coming from the bootstrap analysis, and to which is finally propagated the magnification error (see Section 3.4). Flux and RMS are extracted as indicated in Section 3.1: flux is integrated in the central circular region of the stack stamp, with a radius $R_{\text{integ}} = 2''$, and then converted to Jy from Jy/beam. RMS is computed from the standard deviation in empty stacks. (a) $\langle\mu\rangle$ is the average magnification of the sources in the subsample.

$\langle z \rangle$	$\log(\langle M_* \rangle / M_\odot)$	$\langle \text{Dust Mass} \rangle$ (M_\odot)	Flux (mJy)	RMS (mJy)	$\langle \mu \rangle^{(a)}$
1.42	8.48	$< 2.49 \times 10^6$	–	4.28×10^{-3}	3.43
2.51	8.53	$< 1.82 \times 10^6$	–	5.64×10^{-3}	5.41
3.45	8.54	$< 1.27 \times 10^6$	–	6.51×10^{-3}	7.83
4.47	8.56	$< 9.43 \times 10^5$	–	6.98×10^{-3}	10.55
1.42	9.43	$1.61 \times 10^7 \pm 4.33 \times 10^6$	7.84×10^{-2}	6.67×10^{-3}	3.24
2.54	9.39	$3.89 \times 10^6 \pm 2.54 \times 10^6$	2.54×10^{-2}	8.25×10^{-3}	3.78
3.41	9.41	$4.96 \times 10^6 \pm 2.61 \times 10^6$	4.49×10^{-2}	9.12×10^{-3}	4.64
4.44	9.42	$< 2.19 \times 10^6$	–	9.12×10^{-3}	5.95
1.41	10.42	$6.95 \times 10^7 \pm 1.84 \times 10^7$	0.28	1.27×10^{-2}	2.67
2.46	10.33	$5.57 \times 10^7 \pm 1.78 \times 10^7$	0.3	2.37×10^{-2}	3.16
3.43	10.35	$3.57 \times 10^7 \pm 1.32 \times 10^7$	0.33	1.96×10^{-2}	4.71
4.46	10.37	$1.7 \times 10^7 \pm 1.01 \times 10^7$	0.2	2.02×10^{-2}	5.67
1.41	11.2	$1.02 \times 10^8 \pm 4.17 \times 10^7$	0.39	2.88×10^{-2}	2.53
2.56	11.22	$< 3.58 \times 10^7$	–	9.51×10^{-2}	4.6
3.55	11.38	$< 3.21 \times 10^7$	–	4.93×10^{-2}	2.33
4.46	11.39	$1.55 \times 10^7 \pm 1.11 \times 10^7$	0.16	4.03×10^{-2}	4.87

median dust masses derived through our stacking analyses are systematically slightly lower than the mean dust masses (see Figure 9 for illustration and the appendix for detailed plots). While the median stellar mass and SFR of each subsample are also systematically lower than the mean (see Figures C.1 and C.2), the difference is not big enough to explain the offset dust mass observed between the mean and median stacks. This, again, hints to a possibly skewed distribution of dust mass in each subsample, resulting in offsets between mean and median dust masses. However, it should be however noted that the dust-mass trends

observed in this analysis (with redshift, stellar mass and SFR) remain the same in the median stacking analyses.

5. Discussion

As our analysis focuses on galaxies spanning a large redshift range, and our observation remains at a fixed observed wavelength, it is important to question the assumption made here; that the continuum flux traces the same physical process at a rest wavelength $\lambda_{\text{rest}} \sim 0.5$ mm (corresponding to $z \sim 1$) and $\lambda_{\text{rest}} \sim 0.18$ mm (corresponding to $z \sim 5$). More specifically, the

Table 4. Similar to Table 3 but for SFR subsamples.

$\langle z \rangle$	$\langle \text{SFR} \rangle$ (M_{\odot}/yr)	$\langle \text{Dust Mass} \rangle$ (M_{\odot})	Flux (mJy)	RMS (mJy)	$\langle \mu \rangle$
1.39	0.15	$3.72 \times 10^6 \pm 1.82 \times 10^6$	1.95×10^{-2}	4.28×10^{-3}	3.51
2.51	0.81	$<1.94 \times 10^6$	–	6.17×10^{-3}	5.55
3.45	0.99	$<1.14 \times 10^6$	–	7.17×10^{-3}	9.62
4.47	0.53	$<6.72 \times 10^5$	–	7.05×10^{-3}	14.94
1.45	2.84	$1.78 \times 10^7 \pm 4.96 \times 10^6$	8.13×10^{-2}	6.47×10^{-3}	3.04
2.53	1.79	$<3.17 \times 10^6$	–	7.19×10^{-3}	3.95
3.43	2.16	$6.43 \times 10^6 \pm 2.94 \times 10^6$	5.51×10^{-2}	7.36×10^{-3}	4.38
4.45	4.68	$<2.21 \times 10^6$	–	7.72×10^{-3}	4.97
1.47	24.56	$7.06 \times 10^7 \pm 1.83 \times 10^7$	0.26	1.38×10^{-2}	2.5
2.52	19.66	$3.4 \times 10^7 \pm 1.23 \times 10^7$	0.2	2.29×10^{-2}	3.49
3.4	31.67	$2.64 \times 10^7 \pm 1.05 \times 10^7$	0.22	2.37×10^{-2}	4.23
4.46	10.55	$2.72 \times 10^7 \pm 1.78 \times 10^7$	0.19	2.29×10^{-2}	3.4
1.76	86.71	$2.56 \times 10^8 \pm 1.26 \times 10^8$	1.04	7.88×10^{-2}	2.64
2.09	60.65	$1.8 \times 10^8 \pm 4.46 \times 10^7$	0.65	9.54×10^{-2}	2.25
3.87	81.75	$<6.56 \times 10^7$	–	0.1	2.35
4.58	53.34	$<3.55 \times 10^7$	–	6.11×10^{-2}	2.45
2.84	1.33×10^2	$2.54 \times 10^8 \pm 7.27 \times 10^7$	1.0	0.2	2.17
3.5	1.51×10^2	$<4.71 \times 10^7$	–	6.67×10^{-2}	2.16
4.44	3.52×10^2	$<4.89 \times 10^7$	–	0.1	2.93

Table 5. Fitting results. Fits are performed with function of the form $M_{\text{dust}}(x) = ax^b$ where a and b are free parameters and x is respectively the SFR, z or M_* . The range of applicability refers to the parameter range over which subsamples yielded detections. See Figures B.2 and B.1 to visualize the fits.

$M_{\text{dust}}(\text{SFR})$ (fixed z)			
z range	a	b	Range of applicability
$1 \leq z < 2$	$7.2 \pm 1.2 \times 10^6$	$7.8 \pm 0.7 \times 10^{-1}$	$-1 < \log(\text{SFR}) < 2$
$2 \leq z < 3$	$9.2 \pm 5.7 \times 10^5$	$12.3 \pm 1.5 \times 10^{-1}$	$1 < \log(\text{SFR}) < 3$
$M_{\text{dust}}(z)$ (fixed SFR)			
SFR range (M_{\odot} per year)	a	b	Range of applicability
$10 < \text{SFR} < 50$	$10.5 \pm 1.6 \times 10^7$	-1.1 ± 0.2	$1 \leq z < 5$
$M_{\text{dust}}(M_*)$ (fixed z)			
z range	a	b	Range of applicability
$1 \leq z < 2$	$5.2 \pm 13.0 \times 10^3$	$4.8 \pm 1.1 \times 10^{-1}$	$8 < \log(M_*/M_{\odot}) < 12$
$M_{\text{dust}}(z)$ (fixed M_*)			
M_* range (M_{\odot})	a	b	Range of applicability
$10^9 < M_* < 10^{10}$	$3.0 \pm 1.3 \times 10^7$	-1.8 ± 0.7	$1 \leq z < 4$
$10^{10} < M_* < 10^{11}$	$10.5 \pm 2.7 \times 10^7$	-1.0 ± 0.3	$1 \leq z < 4$

validity of the dust mass equation (see Section 3.3) comes from the assumption that the dust is optically thin, and that the flux measurement probes the Rayleigh-Jeans dust emission –thus the part of the SED that is dominated by the emission of the dust at $T=25\text{K}$, that dominates the dust mass budget. This is true at long wavelengths, where we effectively probe the Rayleigh-Jeans tail of the dust emission (e.g. Magdis et al. 2012; Scoville et al. 2016). However, the higher the redshift observed the closer one gets to the peak of dust emission, more sensitive to temperature and total luminosity. This could explain the low detection rate in the high- z subsamples, even when the number of stack

sources is high –and hence the corresponding RMS in the stack maps is low.

While numerous studies show an evolution of dust temperature with redshift, it is important to distinguish between the peak temperature, which is thought from both theoretical and observational works to increase with redshift (e.g. Magdis et al. 2012; Magnelli et al. 2014; Béthermin et al. 2015; Ferrara et al. 2017; Narayanan et al. 2018; Schreiber et al. 2018; Liang et al. 2019; Ma et al. 2019; Sommovigo et al. 2020), and the mass-weighted temperature, probing the Rayleigh-Jeans tail, which can be directly used to measure the dust mass as stated above. Unlike the peak temperature, the mass-weighted temperature is thought to

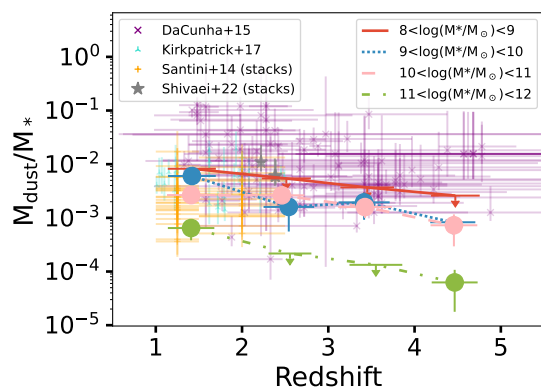


Fig. 5. Average dust mass to average stellar mass ratio as a function of redshift. Similar to the right panel of Figure 4 but normalized by the stellar mass of galaxies in the sample. Error bars combine the error on dust mass computation and stellar mass distribution.

be mostly constant with redshift (see [Scoville et al. 2016](#); [Liang et al. 2019](#)). It should be noted however, that the mass-weighted temperature still exhibits a small range in possible values, typically from 15 to 45 K (e.g. [Liang et al. 2019](#)), and a small increase with redshift may exist. On the other hand, [Dudzevičiūtė et al. \(2020\)](#) argue that the previously observed evolution of the dust temperature is likely due to the luminosity evolution in the samples employed, and suggest a dust temperature of 30.4 ± 0.3 , constant with redshift. In any event, to ease comparison with studies similar to ours and to limit complexity, we decided to keep a fixed temperature at all redshifts for dust mass computations. Consequently, one should note that using $T = 40$ K (instead of 25) in dust masses computation would change our results by $\sim 50\%$ in the highest redshift bin.

When comparing our results to the semi-analytical modeling from [Popping et al. \(2017\)](#); [Lagos et al. \(2019\)](#); [Vijayan et al. \(2019\)](#); [Triani et al. \(2020\)](#), see Figures 10 and 11² we can see an overall decent agreement in dust mass predictions as a function of stellar mass at $z \sim 1$. However, all models but the one presented in [Vijayan et al. \(2019\)](#) predict an overall increase of dust mass with redshift while our analysis shows the opposite. In addition the dust mass derived in the high-mass end of our subsamples is typically smaller than predicted by the models (though this flattening might be due to the presence of quiescent galaxies in our sample, as shown in the appendix). In addition, one should note that the method used for computing the average dust mass in the SHARK model ([Lagos et al. 2019](#)) differs to the one used in this work. To highlight this difference we show, on Figures 10 and 11, both the average dust masses predicted by the SHARK model and the dust masses computed, using equation 1, from the band 6 continuum (S6) predicted by SHARK. It is interesting to note that at $z \sim 3$ and at $z \sim 5$ the dust mass derived using the predicted S6 differs by almost one dex from the dust mass otherwise predicted. As mentioned above, this might be a direct consequence of the evolution of the rest-wavelength with redshift, moving observation closer to the peak of dust emission. Surprisingly however, our results seem in bet-

ter agreement with the direct dust mass measurements compared to the ones obtained from S6.

As the analysis relies on photometric redshifts for a large fraction of the catalog, it is important to consider the potential impact this could have on the results. In particular, it should be noted that the bins at $z > 3$ appear overpopulated. This can be seen on Figure 3, when comparing the SMF of our sample to the SMF of the COSMOS2020 sample [Weaver et al. \(2022a,b\)](#). As a consequence the dust content at $z > 3$ is likely over-estimated. This is probably due to the miss-classification of some lower redshift sources to higher redshift, as suggested in [Kokorev et al. \(2022\)](#) and mentioned in Section 2.2.

It should also be noted that, because the catalog used was generated using *HST* and *Spitzer* photometry, some of the most dusty galaxies may be missing, biasing the analysis toward lower averaged dust masses. Indeed, as pointed out in [Kokorev et al. \(2022\)](#), from the 180 sources individually detected with a SNR > 4 in the ALCS data, only 145 are identified in their catalog, indicating that some of the most dusty galaxies may be missed from our analysis. This bias could be strongest in the high-redshift bins, where only the UV-brightest galaxies (i.e. typically less dust-obscured) might be observed. The use of James-Webb Space Telescope (JWST)-based catalogs could help to include more of the missed dusty galaxies, especially at high- z , and to improve the SED fitting routines.

As shown in the appendix (Figures A.1 and A.2), the inclusion of quiescent galaxies in the stacks biases the analysis toward lower dust masses, especially in the samples split through stellar-mass. This highlights that some sources included in the high-mass subsamples have low SFR and also low dust masses. The higher average dust mass observed in the mass-selected samples when excluding sources with $\Delta MS < -0.5$, and on the other hand, the relatively stable average dust mass in SFR selected samples, implies that SFR should be a better dust mass tracer. It shows in addition that quiescent galaxies will have a typically lower dust content than their star forming counterparts at similar stellar mass.

As in [Magnelli et al. \(2020\)](#), we use the dust opacities from [Li & Draine \(2001\)](#) to derive the dust masses. Those values have been constrained from observations of the diffuse interstellar medium (ISM) and therefore these properties are representative for dust in the diffuse ISM. However, some studies in nearby galaxies (e.g. [Galliano et al. 2018](#)) showed that the opacity from [Li & Draine \(2001\)](#) has perhaps been underestimated by a factor of 2 – 3. One must emphasise that larger values of opacities in galaxies does not mean that the values of [Li & Draine \(2001\)](#) are wrong. Their values have been constrained for the diffuse interstellar medium and are therefore well adapted for galaxies only if the bulk of dust emission emerges from the diffuse interstellar medium of galaxies. The underestimation of the dust opacity might indicate that the majority of the dust emission does not emerge from diffuse regions but from denser regions where dust grains are likely to be larger.

In dense regions of the ISM, dust grains grow through accretion and coagulation which triggers an increase in the dust opacity by a factor 2 – 3 (e.g. [Köhler et al. 2015](#)). The underestimation of the dust opacities in some nearby galaxies could therefore mean that the bulk of the dust emission arises from dense regions where dust grains are larger than in the diffuse ISM. This seems to be also the case in high-redshift galaxies as [Magnelli et al. \(2020\)](#) claim that the bulk of the dust emission in their galaxy sample emerges from the molecular phase and therefore dense regions where dust differs from the diffuse ISM. They also stated that there could be a significant increase in the dust emis-

² One should note that the SHARK model ([Lagos et al. 2019](#)) does not directly track the buildup and destruction of dust. Instead, dust masses are estimated assuming an empirical $z = 0$ relation between dust-to-gas ratio and gas-phase metallicity.

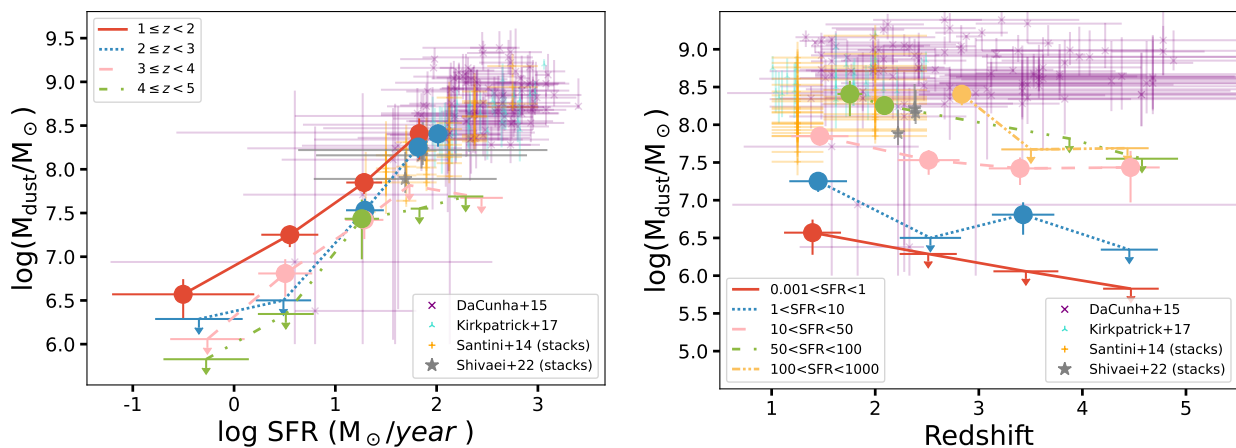


Fig. 6. Similar to Figure 4 but in SFR bins instead of stellar mass.

sivity from diffuse to denser regions which can be explained in terms of grain growth (e.g. Köhler et al. 2015).

There is for now no consensus on the dust properties one must consider, neither in nearby nor in high-redshift galaxies. Moreover, dust grains are unlikely to be the same within galaxies and from one galaxy to another, which adds to the complexity. Although diffuse ISM-like dust grains might not be responsible for the majority of the dust emission in galaxies, these dust models have the advantage of being thoroughly developed and extensively used. We therefore use those dust properties from the diffuse ISM until we have more constraints on the dust grains responsible for the emission in these galaxies.

6. Summary

We used deep ALMA band 6 data, over 33 lensing clusters, to perform a set of stacking analyses on a large sample of 4103 lensed sources, whose positions and physical parameters were extracted from the HST/IRAC catalog presented in Kokorev et al. (2022). Spanning redshifts from $z = 1$ to $z = 5$, SFRs from $0.001 M_{\odot} \text{ yr}^{-1}$ to $1000 M_{\odot} \text{ yr}^{-1}$ and stellar masses from $10^8 M_{\odot}$ to $10^{12} M_{\odot}$. To study the evolution of the dust mass through cosmic time, we binned the sources in five different redshifts bins, and further also grouped sources according to their SFR and stellar mass, respectively. We performed continuum stacking on each of the subsamples using LINESTACKER (Jolly et al. 2020).

Using the mean continuum stacked flux, we computed average dust masses. From the non detections we derive 3σ upper limits. Using both detections and upper limits we study the evolution trend of dust mass with redshift. We see clear indications for average dust mass diminution with redshift. Similarly we study the evolution of dust mass with stellar mass and SFR, in both cases we see a positive correlation. From our detections we derived relationships between dust mass and SFR or stellar mass in different redshift range. The results from our study are mostly consistent with results from modeling (at least at $z \sim 1$) and from other similar studies. Our analysis allows us to probe regimes of stellar mass and SFR unexplored so far. The highest redshift bin shows mostly non-detections, and the corresponding upper limits indicate low average dust masses –even though the overall RMS is low– when compared to other studies. This could be due to the different rest-wavelength probed at high- z , lying closer to the peak of dust emission. Or to the tendency of

individual high- z dust measurements to be biased towards very dust-bright objects.

The linear trends observed between stellar mass and dust mass confirm that as galaxies evolve and form more stars, they also accumulate more dust. These dust grains play a vital role in catalyzing the formation of H_2 , thus influencing the overall gas reservoir available for future star formation. Dust becomes an integral component of a self-perpetuating cycle, accumulating throughout the stars’ life cycle and subsequently bolstering the SFR. In addition the inverse trend observed between average dust-mass and redshift, implies that the build-up of dust in galaxies over cosmic-time is a gradual process, aligning with the overall evolution of the SFR density (e.g Magnelli et al. 2020). This further hints for a gradual increase of the average-metallicity in galaxies with cosmic time, as dust grains are known to be composed of heavy-elements produced in stars.

Acknowledgements. The authors thank the anonymous reviewer for their thoughtful and constructive suggestions, which greatly helped improve this manuscript. This paper makes use of the ALMA data: ALMA #2018.1.00035.L, #2013.1.00999.S, and #2015.1.01425.S. ALMA is a partnership of the ESO (representing its member states), NSF (USA) and NINS (Japan), together with NRC (Canada), MOST and ASIAA (Taiwan), and KASI (Republic of Korea), in cooperation with the Republic of Chile. The Joint ALMA Observatory is operated by the ESO, AUI/NRAO, and NAOJ. JBJ thanks Ian Smail for the discussion. KK acknowledges support from the Swedish Research Council (2015-05580), and the Knut and Alice Wallenberg Foundation (KAW 2020.0081). K. Kohno acknowledges the JSPS KAKENHI Grant Number JP17H06130 and the NAOJ ALMA Scientific Research Grant Number 2017-06B. AG acknowledges funding from ANID-Chile NCN2023_002 and FONDECYT Regular 1171506. DE acknowledges support from a Beatriz Galindo senior fellowship (BG20/00224) from the Spanish Ministry of Science and Innovation, projects PID2020-114414GB-I00 and PID2020-113689GB-I00 financed by MCIN/AEI/10.13039/501100011033, project P20_00334 financed by the Junta de Andalucía, project A-FQM-510-UGR20 of the FEDER/Junta de Andalucía-Consejería de Transformación Económica, Industria, Conocimiento y Universidades. FEB acknowledges support from ANID-Chile BASAL CATA FB210003, FONDECYT Regular 1200495 and 1190818, and Millennium Science Initiative Program – ICN12_009.

References

- Aravena, M., Boogaard, L., González-López, J., et al. 2020, ApJ, 901, 79
 Bertoldi, F., Carilli, C. L., Cox, P., et al. 2003, A&A, 406, L55
 Béthermin, M., Daddi, E., Magdis, G., et al. 2015, A&A, 573, A113
 Béthermin, M., Fudamoto, Y., Ginolfi, M., et al. 2020, A&A, 643, A2
 Birkin, J. E., Weiss, A., Wardlow, J. L., et al. 2021, MNRAS, 501, 3926
 Bouwens, R., González-López, J., Aravena, M., et al. 2020, ApJ, 902, 112
 Casey, C. M. 2012, MNRAS, 425, 3094
 Casey, C. M., Narayanan, D., & Cooray, A. 2014, Physics Reports, 541, 45–161

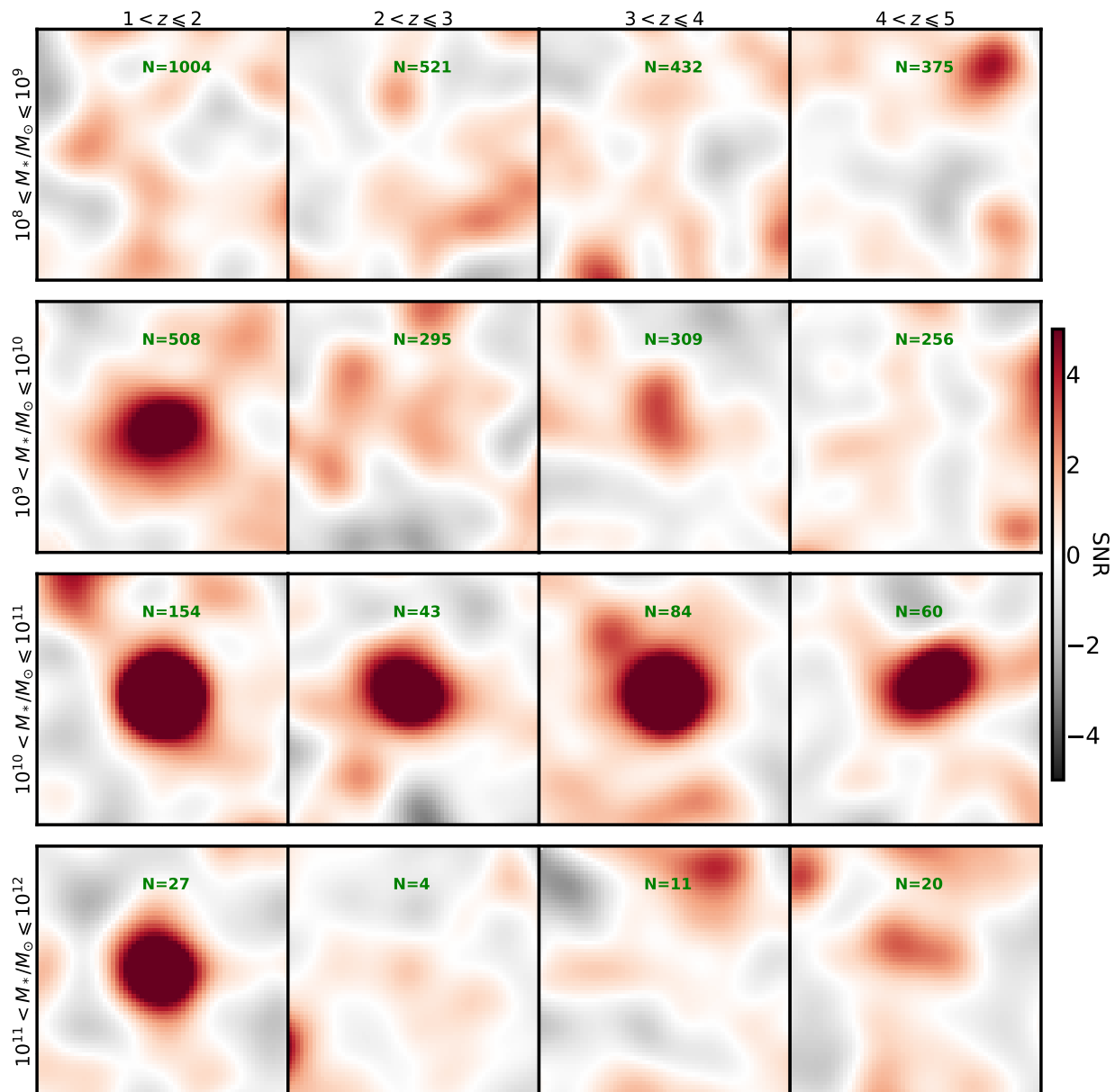


Fig. 7. 9.76×9.76 arcsec² (61×61 pixels) mean-stacking stamps, split in bins of stellar mass and redshift. Each map is normalised by the corresponding standard deviation computed in associated empty stacks (see Section 3.1). The number of sources stacked (N) is indicated for each bin.

- Chapin, E. L., Pope, A., Scott, D., et al. 2009, MNRAS, 398, 1793
 Coe, D., Salmon, B., Bradač, M., et al. 2019, ApJ, 884, 85
 Combes, F. 2018, A&A Rev., 26, 5
 da Cunha, E., Eminian, C., Charlot, S., & Blaizot, J. 2010, MNRAS, 403, 1894
 da Cunha, E., Groves, B., Walter, F., et al. 2013, ApJ, 766, 13
 da Cunha, E., Walter, F., Smail, I. R., et al. 2015, ApJ, 806, 110
 Draine, B. T. 2011, Physics of the Interstellar and Intergalactic Medium
 Draine, B. T., Dale, D. A., Bendo, G., et al. 2007, ApJ, 663, 866
 Driver, S. P., Andrews, S. K., da Cunha, E., et al. 2018, MNRAS, 475, 2891
 Dudzevičiūtė, U., Smail, I., Swinbank, A. M., et al. 2021, MNRAS, 500, 942
 Dudzevičiūtė, U., Smail, I., Swinbank, A. M., et al. 2020, MNRAS, 494, 3828
 Engelbracht, C. W., Rieke, G. H., Gordon, K. D., et al. 2008, ApJ, 678, 804
 Faisst, A. L., Fudamoto, Y., Oesch, P. A., et al. 2020, MNRAS, 498, 4192
 Ferrara, A., Hirashita, H., Ouchi, M., & Fujimoto, S. 2017, MNRAS, 471, 5018
 Fujimoto, S., Kohno, K., Ouchi, M., et al. 2023, arXiv e-prints, arXiv:2303.01658
 Galametz, M., Madden, S. C., Galliano, F., et al. 2011, A&A, 532, A56
 Galliano, F., Galametz, M., & Jones, A. P. 2018, Annual Review of Astronomy and Astrophysics, 56, 673
 González-López, J., Bauer, F. E., Romero-Cañizales, C., et al. 2017, A&A, 597, A41
 González-López, J., Novak, M., Decarli, R., et al. 2020, ApJ, 897, 91
 Guerrero, A., Nagar, N., Kohno, K., et al. 2023, MNRAS, 526, 2423
 Hodge, J. A. & da Cunha, E. 2020, Royal Society Open Science, 7, 200556
 Hunt, L., Bianchi, S., & Maiolino, R. 2005, A&A, 434, 849
 Jolly, J.-B., Knudsen, K. K., & Stanley, F. 2020, MNRAS, 499, 3992
 Kirkpatrick, A., Pope, A., Sajina, A., et al. 2017, ApJ, 843, 71
 Knudsen, K. K., Richard, J., Kneib, J.-P., et al. 2016, MNRAS, 462, L6
 Kohno, K., Fujimoto, S., Tsujita, A., et al. 2023, arXiv e-prints, arXiv:2305.15126
 Kokorev, V., Brammer, G., Fujimoto, S., et al. 2022, arXiv e-prints, arXiv:2207.07125
 Kovács, A., Omont, A., Beelen, A., et al. 2010, ApJ, 717, 29
 Köhler, M., Ysard, N., & Jones, A. P. 2015, Astronomy and Astrophysics, 579, A15
 Lagos, C. d. P., Robotham, A. S. G., Trayford, J. W., et al. 2019, MNRAS, 489, 4196
 Laporte, N., Ellis, R. S., Boone, F., et al. 2017, ApJ, 837, L21
 Li, A. & Draine, B. T. 2001, ApJ, 554, 778
 Li, Q., Narayanan, D., & Davé, R. 2019, MNRAS, 490, 1425
 Liang, L., Feldmann, R., Kereš, D., et al. 2019, MNRAS, 489, 1397

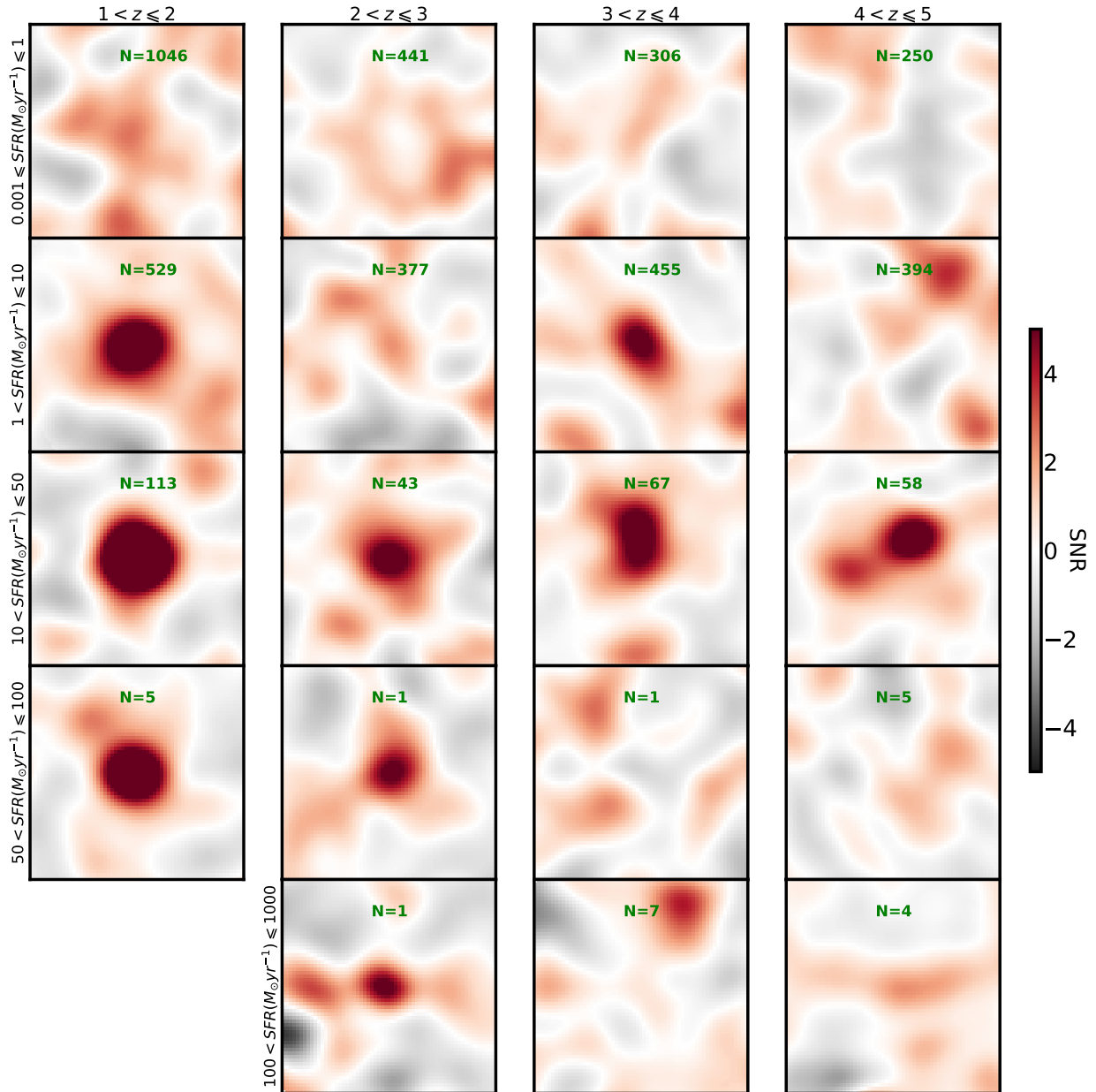


Fig. 8. Similar to Figure 7 but using SFR bins instead of stellar mass ones.

Lotz, J. M., Koekemoer, A., Coe, D., et al. 2017, *ApJ*, 837, 97
Ma, X., Hayward, C. C., Casey, C. M., et al. 2019, *MNRAS*, 487, 1844
Magdis, G. E., Daddi, E., Béthermin, M., et al. 2012, *ApJ*, 760, 6
Magnelli, B., Boogaard, L., Decarli, R., et al. 2020, *ApJ*, 892, 66
Magnelli, B., Lutz, D., Saintonge, A., et al. 2014, *A&A*, 561, A86
Magnelli, B., Lutz, D., Santini, P., et al. 2012, *A&A*, 539, A155
Magrini, L., Bianchi, S., Corbelli, E., et al. 2011, *A&A*, 535, A13
McMullin, J. P., Waters, B., Schiebel, D., Young, W., & Golap, K. 2007, in *Astronomical Society of the Pacific Conference Series*, Vol. 376, *Astronomical Data Analysis Software and Systems XVI*, ed. R. A. Shaw, F. Hill, & D. J. Bell, 127
Narayanan, D., Davé, R., Johnson, B. D., et al. 2018, *MNRAS*, 474, 1718
Orellana, G., Nagar, N. M., Elbaz, D., et al. 2017, *A&A*, 602, A68
Planck Collaboration, Abergel, A., Ade, P. A. R., et al. 2011, *A&A*, 536, A21
Popping, G. & Péroux, C. 2022, *MNRAS*, 513, 1531
Popping, G., Shivaeei, I., Sanders, R. L., et al. 2023, *A&A*, 670, A138
Popping, G., Somerville, R. S., & Galametz, M. 2017, *MNRAS*, 471, 3152
Postman, M., Coe, D., Benítez, N., et al. 2012, *ApJS*, 199, 25
Pozzi, F., Calura, F., Fudamoto, Y., et al. 2021, *arXiv e-prints*, arXiv:2105.14789
Pozzi, F., Calura, F., Zamorani, G., et al. 2020, *MNRAS*, 491, 5073
Rémy-Ruyer, A., Madden, S. C., Galliano, F., et al. 2014, *A&A*, 563, A31
Saintonge, A., Lutz, D., Genzel, R., et al. 2013, *ApJ*, 778, 2

Santini, P., Maiolino, R., Magnelli, B., et al. 2014, *A&A*, 562, A30
Schreiber, C., Glazebrook, K., Nanayakkara, T., et al. 2018, *A&A*, 618, A85
Scoville, N., Aussel, H., Sheth, K., et al. 2014, *ApJ*, 783, 84
Scoville, N., Lee, N., Vanden Bout, P., et al. 2017, *ApJ*, 837, 150
Scoville, N., Sheth, K., Aussel, H., et al. 2016, *ApJ*, 820, 83
Scoville, N. Z. 2013, *Evolution of star formation and gas*, ed. J. Falcón-Barroso & J. H. Knapen, 491
Shapley, A. E., Cullen, F., Dunlop, J. S., et al. 2020, *ApJ*, 903, L16
Shivaeei, I., Popping, G., Rieke, G., et al. 2022, *ApJ*, 928, 68
Sommovigo, L., Ferrara, A., Pallottini, A., et al. 2020, *MNRAS*, 497, 956
Speagle, J. S., Steinhardt, C. L., Capak, P. L., & Silverman, J. D. 2014, *ApJS*, 214, 15
Sun, F., Egami, E., Fujimoto, S., et al. 2022, *ApJ*, 932, 77
Tacconi, L. J., Genzel, R., & Sternberg, A. 2020, *ARA&A*, 58, 157
Tamura, Y., C. Bakx, T. J. L., Inoue, A. K., et al. 2023, *ApJ*, 952, 9
Tamura, Y., Mawatari, K., Hashimoto, T., et al. 2019, *ApJ*, 874, 27
Triani, D. P., Sinha, M., Croton, D. J., Pacifici, C., & Dwek, E. 2020, *MNRAS*, 493, 2490
Valiante, R., Schneider, R., Bianchi, S., & Andersen, A. C. 2009, *MNRAS*, 397, 1661
Venemans, B. P., McMahon, R. G., Walter, F., et al. 2012, *ApJ*, 751, L25
Vijayan, A. P., Clay, S. J., Thomas, P. A., et al. 2019, *MNRAS*, 489, 4072

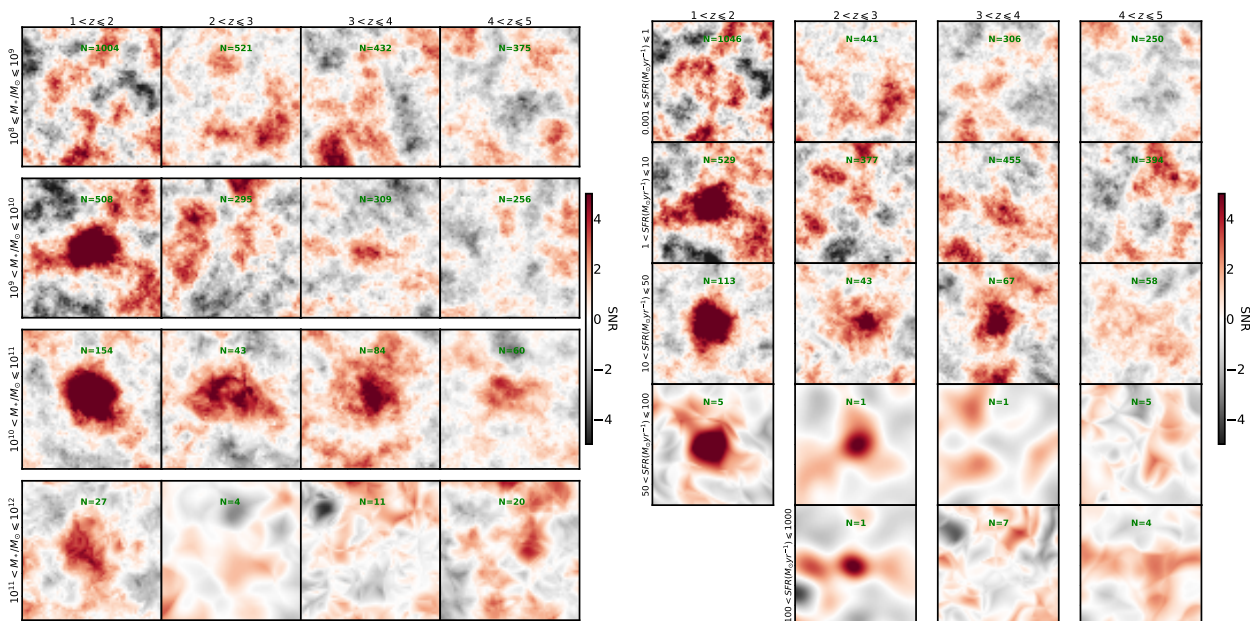


Fig. 9. Median stacking stamps, split in stellar mass and redshift (left panel) and SFR and redshift (right panel). Similar to Figures 7 and 8.

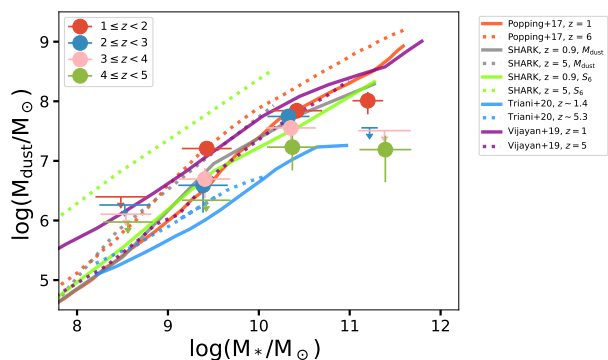


Fig. 10. Log average dust mass recovered as a function of the (log) stellar mass, in each redshift bin. Circles represent detections (above 3σ) while 3σ upper limits are represented by down pointing arrows. Overplotted, the $z = 1$ and $z = 6$ dust mass–stellar mass relation from Popping et al. (2017) and the $z \sim 1$ and $z \sim 5$ relations from Lagos et al. (2019) (SHARK model), Triani et al. (2020), Vijayan et al. (2019). Both the average dust mass directly predicted by the SHARK model, and the dust mass computed from the predicted band 6 flux –following equation 1– are shown.

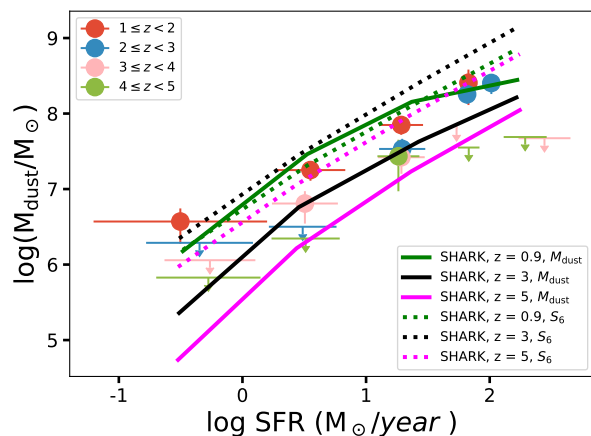


Fig. 11. Similar to Figure 10 but for SFR instead of stellar mass. Prediction from Lagos et al. (2019, SHARK model) at $z \sim 1, 3$ and 5 are shown, both in terms of direct dust mass predictions and dust mass inferred from predicted band 6 flux –following equation 1.

- Wakelam, V., Bron, E., Cazaux, S., et al. 2017, *Molecular Astrophysics*, 9, 1
 Walter, F., Decarli, R., Aravena, M., et al. 2016, *ApJ*, 833, 67
 Watson, D., Christensen, L., Knudsen, K. K., et al. 2015, *Nature*, 519, 327
 Weaver, J. R., Davidzon, I., Toft, S., et al. 2022a, arXiv e-prints, arXiv:2212.02512
 Weaver, J. R., Kauffmann, O. B., Ilbert, O., et al. 2022b, *ApJS*, 258, 11
 Zavala, J. A., Casey, C. M., Manning, S. M., et al. 2021, *ApJ*, 909, 165

Appendix A: Stack excluding quiescent galaxies

As shown on Figure 2 the sample is biased toward sources below the main sequence. To make sure that quiescent galaxies do not bias our analysis and the derived average dust masses, we repeat our stacking analysis after removing all sources with $\Delta MS < -0.5$. In total, 2157 galaxies are removed from the sample, leading to a final size of 1946 after removing quiescent galaxies. The results are shown on Figures A.1 and A.2.

The main difference appear on the stellar mass subsamples, where the derived dust masses are overall higher –especially in the high-stellar mass regime– after excluding quiescent galaxies (although some bins appear now undetected, likely due to the lower number of sources stacked). This suggest that quiescent galaxies may be overall more dust-poor at given stellar mass, driving the average down when included in the entire sample. In any event, the overall trends observed in the main analysis seem to be confirmed even when removing sources with $\Delta MS < -0.5$. One can note that our dust mass measurements are also in better agreement with previous individual results when quiescent galaxies are excluded from the stacks.

Appendix B: Fit results

On Figures B.1 and B.2 are shown the average dust mass recovered as function of stellar mass, SFR or redshift, superposed with the corresponding fit. Only the detections (i.e. S/N above 3σ , see Section 3) are shown and used in the fit. The coefficients of the fits are shown on Table 5.

Appendix C: Distribution of SFR and stellar mass in the subsamples

On Figures C.1 and C.2 are shown the distribution of stellar mass and SFR in the different subsamples. The mean and median values for each subsamples are also shown as red and black vertical lines respectively.

Appendix D: Bootstrapping results

On Figures D.1 and D.2 we show the distribution of the results from our bootstrapping analyses. For each subsample, 1000 new subsamples are randomly selected (see Jolly et al. 2020, for a detailed description of the bootstrapping tool included in LINES-TACKER and used here), and their stack values are collected. The distribution of these stack results (normalized to the original stack result of the corresponding subsample) are shown. Color coding is used to distinguish between the detected (in cyan) and not detected (in red) subsamples. A vertical line is placed at $x = 1$ to guide the eye.

Appendix E: Dust mass inferred from median stacking

In addition to the mean stacking analyses we performed median stacking for each of the subsamples, in the same way as described in the main analysis. The median stacking stamps are shown on Figure 9 and here we show the dust mass evolution as a function of stellar mass and redshift (Figure E.1) and as a function of SFR and redshift (Figure E.2), similar to Figures 4 and 6. While the median stacking analyses show typically lower dust masses (indicating possible skewed distributions) the results and trends are overall very consistent with the mean stacking analyses.

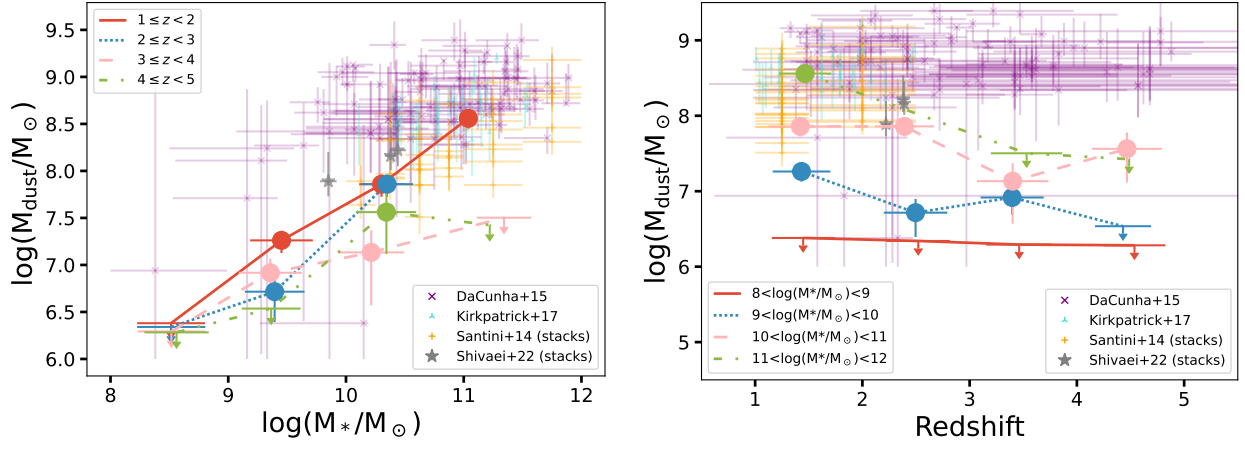


Fig. A.1. Similar to Figure 4 but all sources with $\Delta MS < -0.5$ are excluded. Error bars are computed in the same way as on Figure 4.

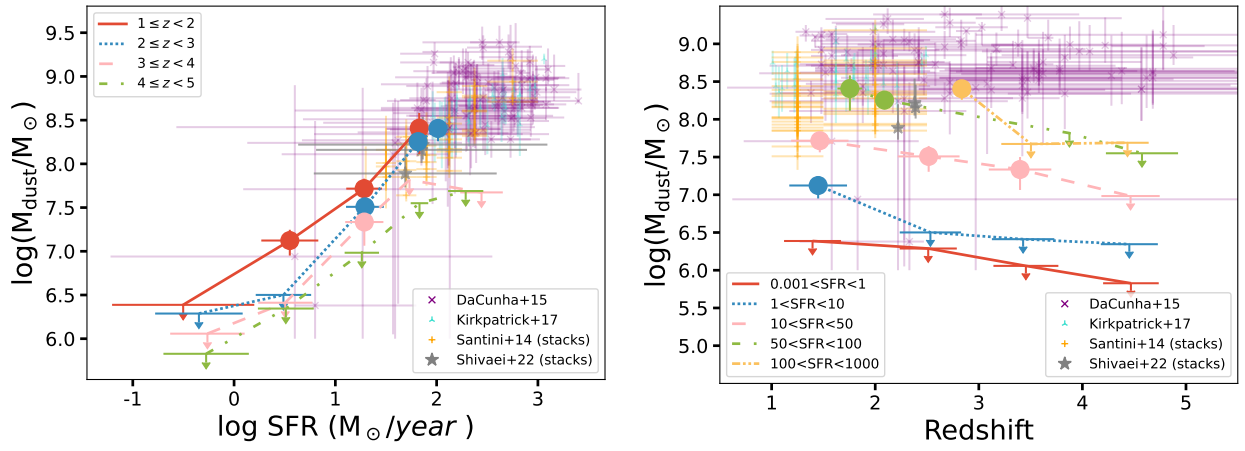


Fig. A.2. Similar to Figure A.1 but for SFR instead of stellar mass.

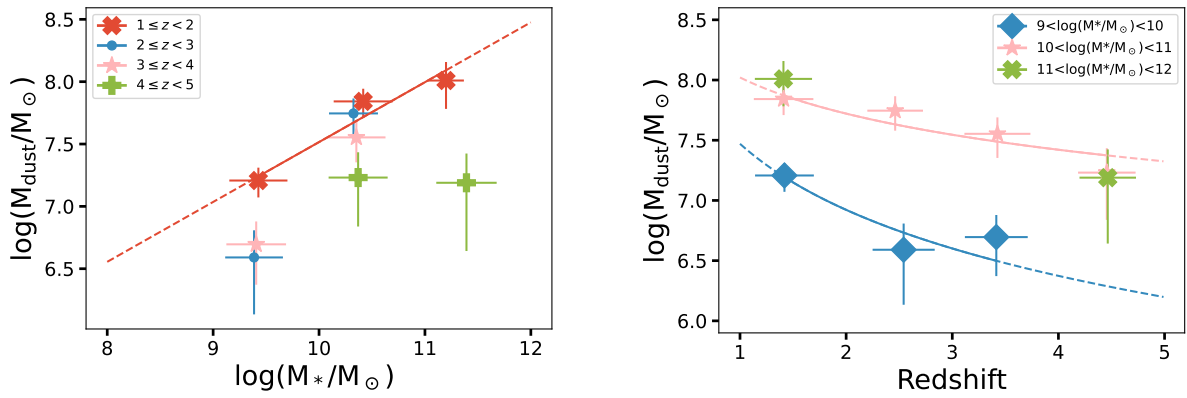


Fig. B.1. Similar to Figure 4 the corresponding fits are also plotted. Only detections (S/N above 3σ) are shown on the plot, and fits are only computed for subsamples with three or more data points (similarly for stellar mass subsample, right panel). Fits are plotted with a continuous (dashed) line when within (outside) the data points range.

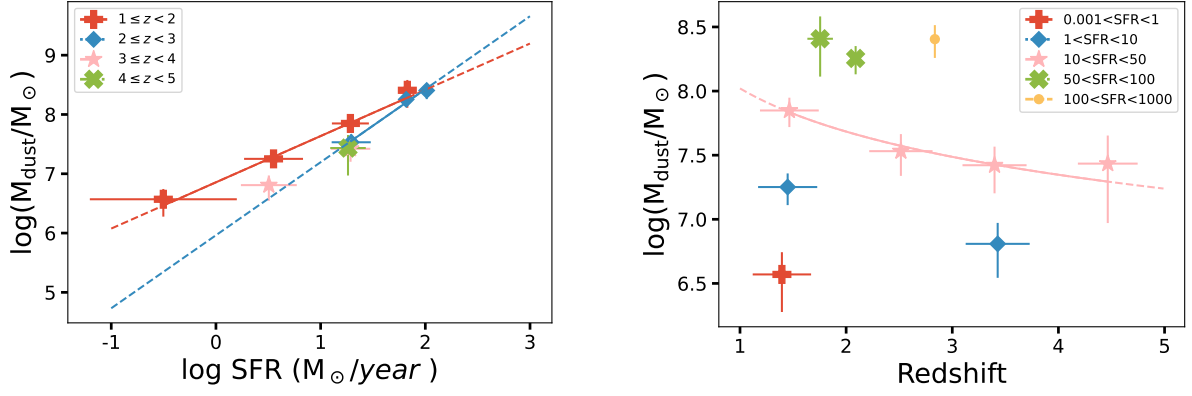


Fig. B.2. Similar to Figure B.1 but for SFR instead of stellar mass.

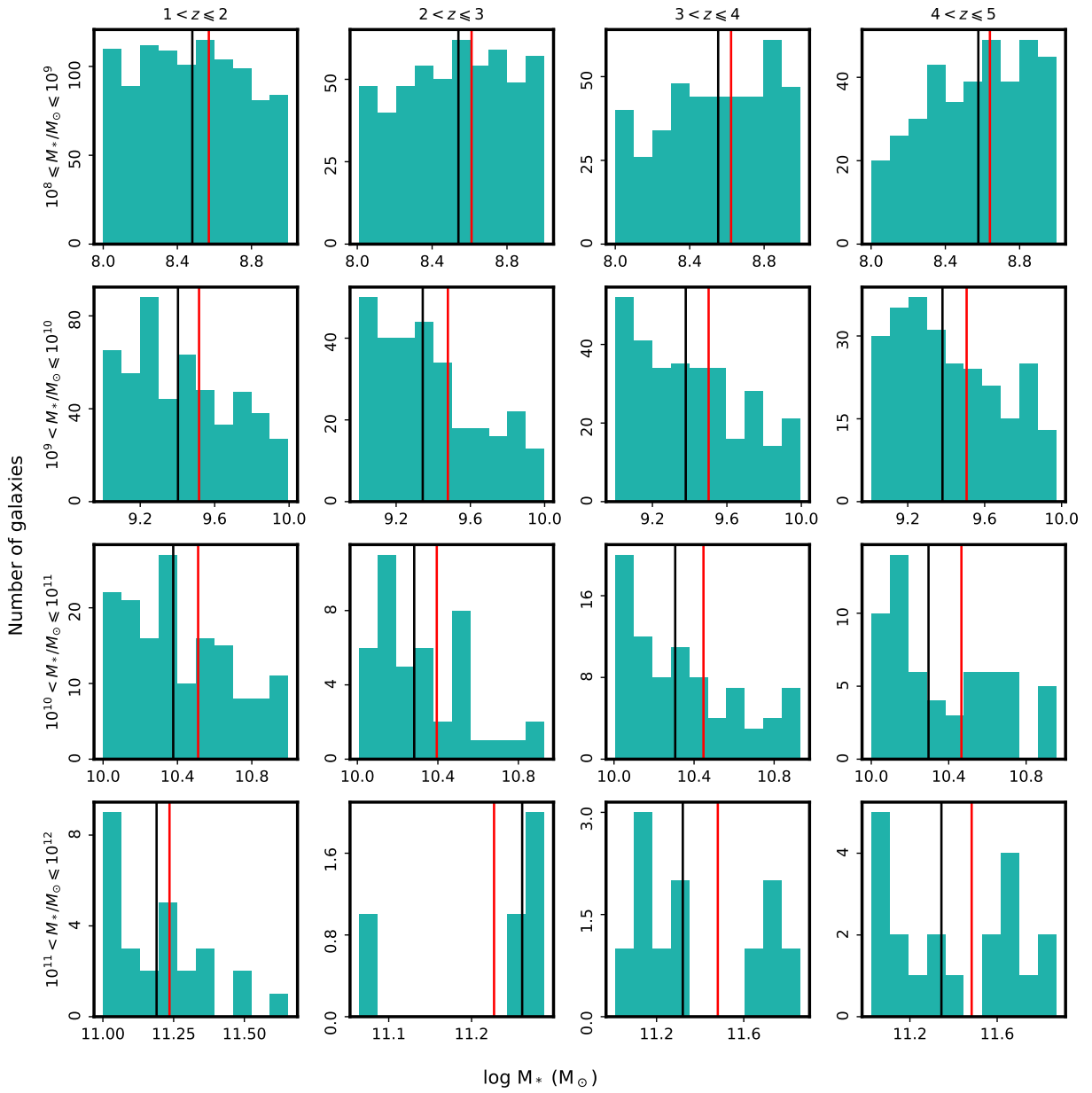


Fig. C.1. Distribution of the (log) stellar mass of galaxies in each subsamples. The red (black) vertical line indicates the mean (median) stellar mass of the subsample.

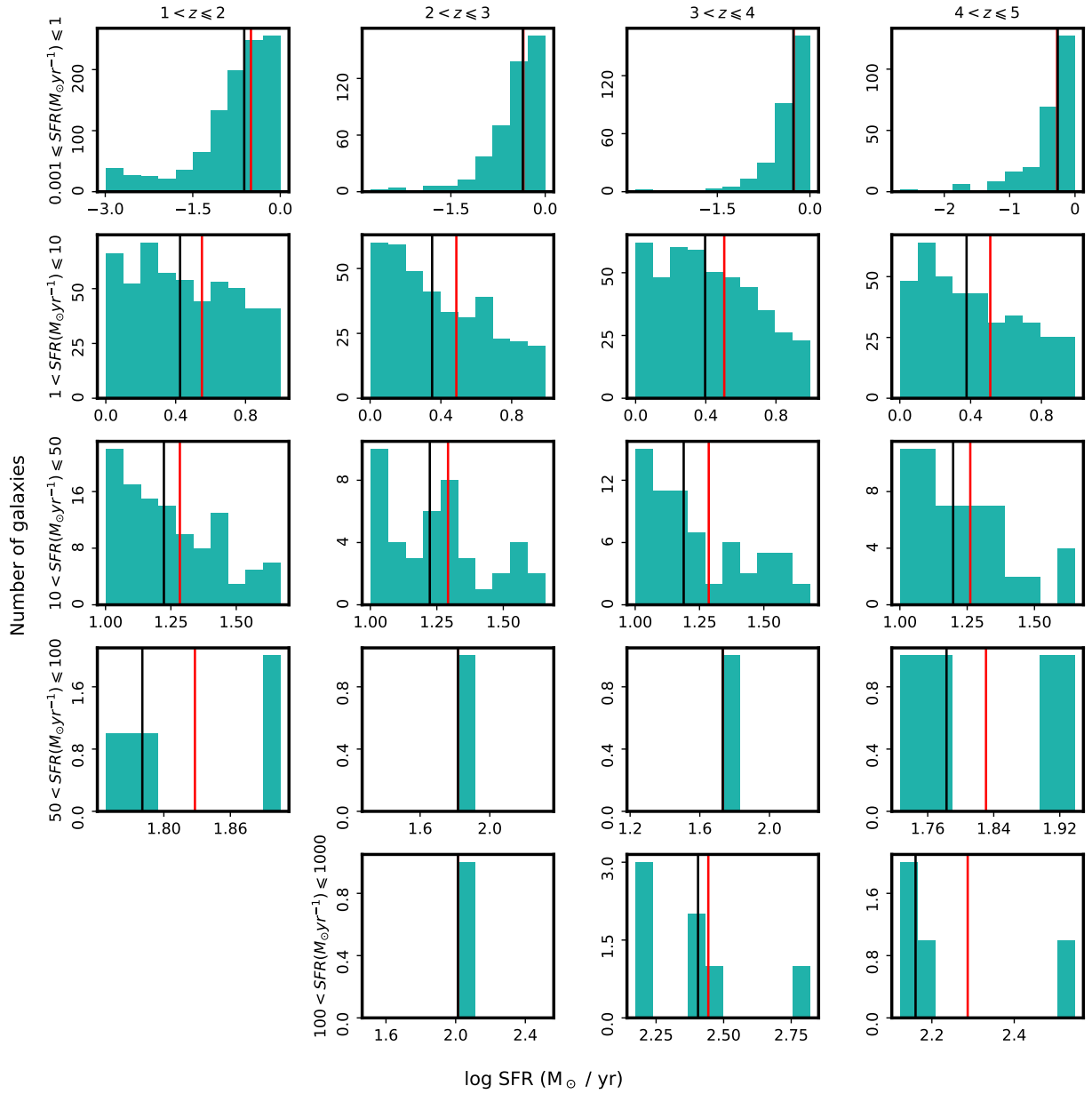


Fig. C.2. Similar to Figure B.1 but for SFR instead of stellar mass.

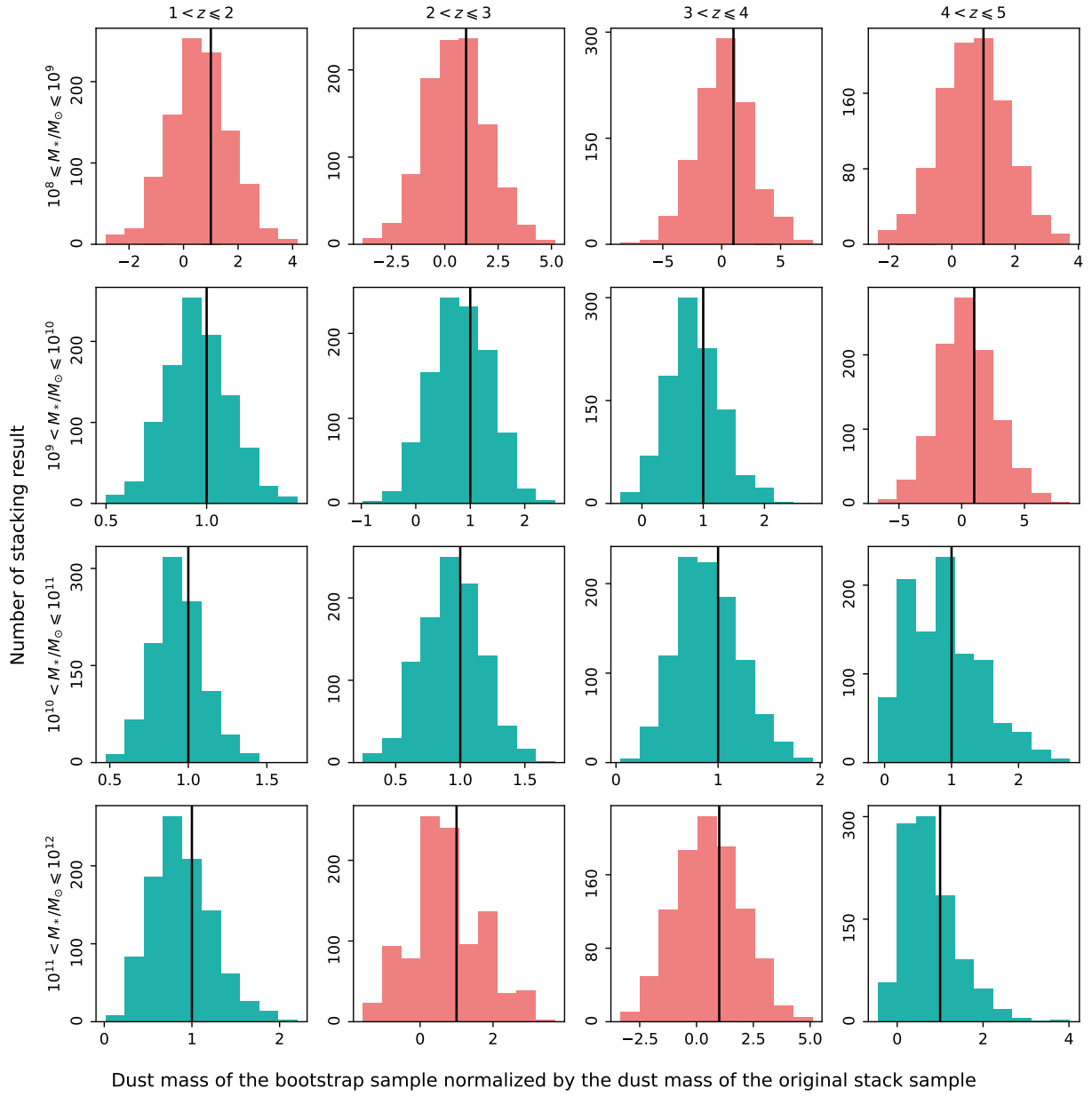


Fig. D.1. Distribution of the bootstrap stack results, normalized by the dust mass of the original stack. Black vertical lines at $x=1$ indicate the expected location of the peak distribution. Histograms in cyan (red) represents the subsample for which the signal was higher (lower) than 3σ .

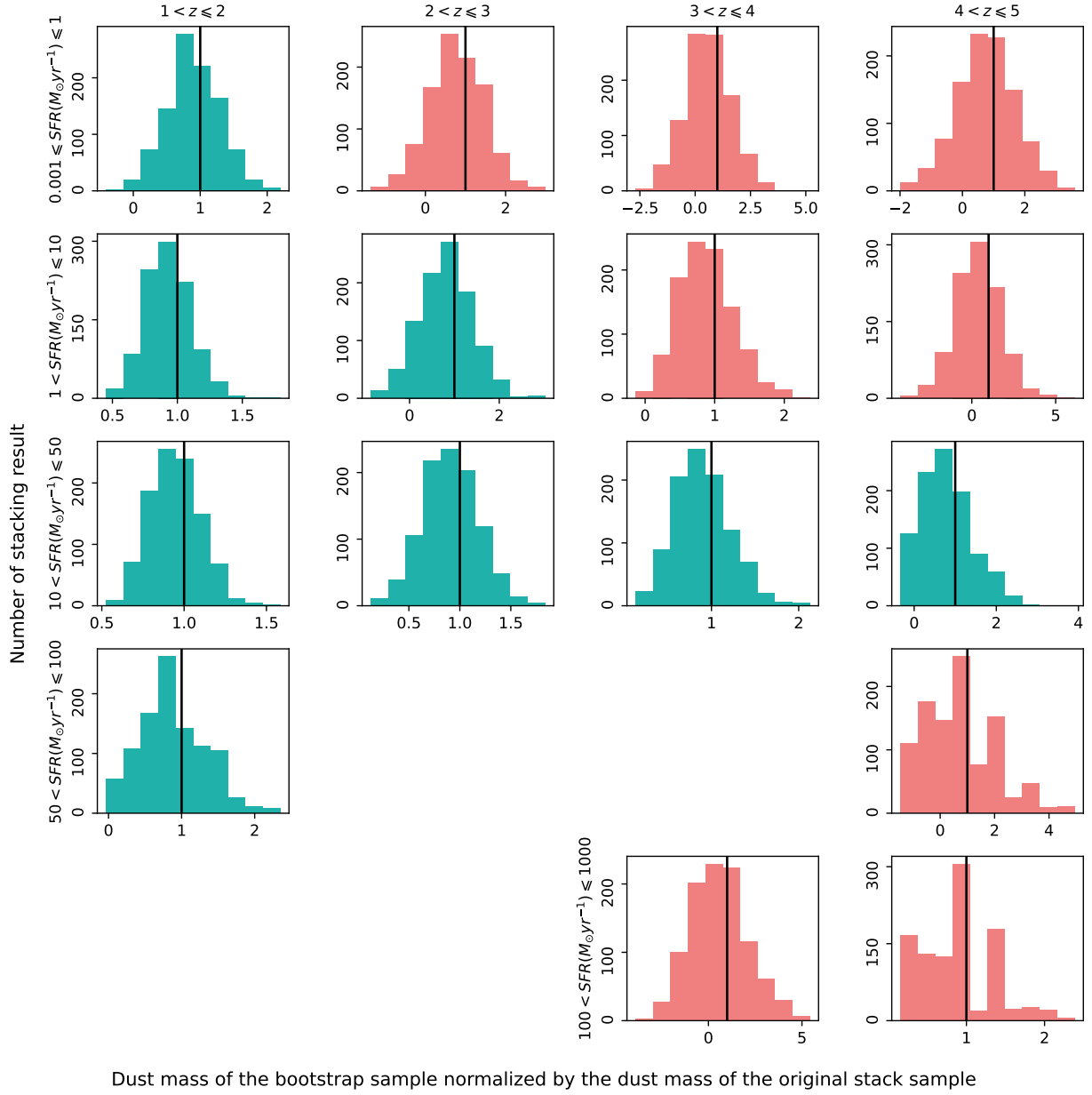


Fig. D.2. Similar to Figure D.1 but for the SFR subsamples. The 3 subsamples containing only 1 source were excluded from this analysis.

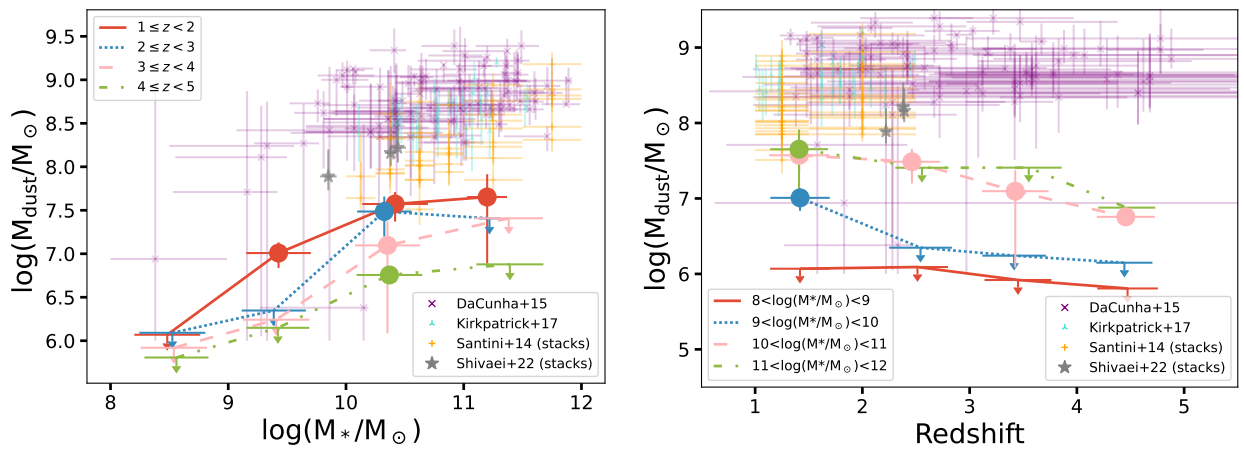


Fig. E.1. Similar to Figure 4 but using median stacking.

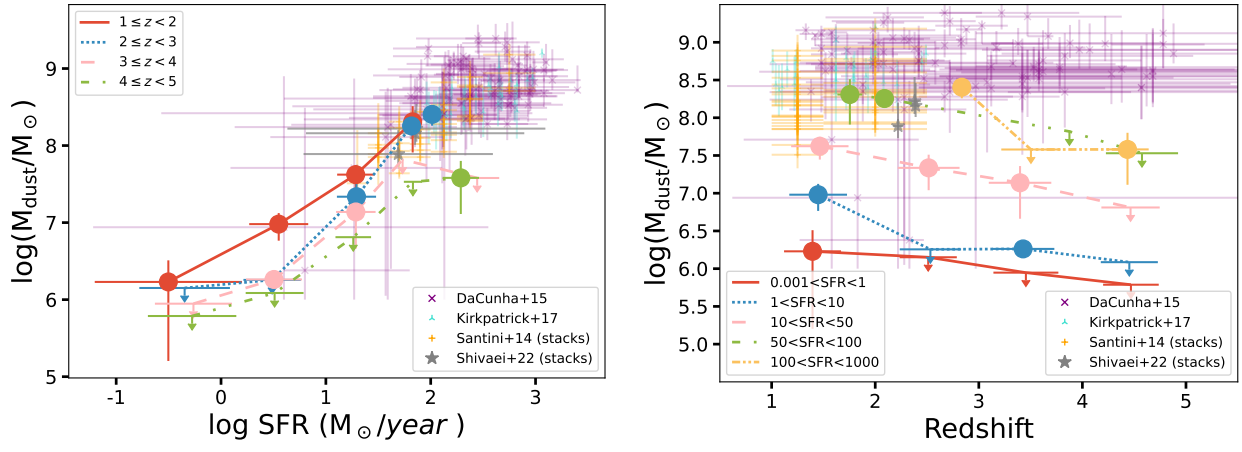


Fig. E.2. Similar to Figure E.1 but for SFR instead of stellar mass.